

1 **Novel approach for health monitoring of earthen embankments**

2
3
4 Utili S. ¹, Castellanza R. ², Galli A. ³, Sentenac P. ⁴,

5
6 *1 School of Engineering*
7 *University of Warwick, UK*
8 *formerly at University of Oxford, UK*
9

10
11 *2 Department of Geology and Geotechnologies*
12 *Università Milano-Bicocca, Italy*
13

14
15 *3 Department of Structural Engineering*
16 *Politecnico di Milano, Italy*
17

18
19 *4 Department of Civil Engineering*
20 *University of Strathclyde, UK*
21

22
23 **ABSTRACT.** This paper introduces a novel modular approach for the monitoring of
24 desiccation-induced deterioration in earthen embankments (levees), which are typically
25 employed as flood defence structures. The approach is based on the use of a combination of
26 geotechnical and non-invasive geophysical probes for the continuous monitoring of the water
27 content in the ground. The level of accuracy of the monitoring is adaptable to the available
28 financial resources.

29 The proposed methodology was used and validated on a recently built 2 km long river
30 embankment in Galston (Scotland, UK). A suite of geotechnical probes was installed to
31 monitor the seasonal variation of water content over a two-year period. Most devices were
32 calibrated in-situ. A novel procedure to extrapolate the value of water content from the
33 geotechnical and geophysical probes in any point of the embankment is illustrated.

34 Desiccation fissuring degrades the resistance of embankments against several failure
35 mechanisms. An index of susceptibility is here proposed. The index is a useful tool to assess
36 the health state of the structure and prioritise remedial interventions.

38
39
40
41

KEY WORDS: embankments; earthfills; resilient infrastructures; geophysics; slope stability; desiccation fissuring.

42 **1. Introduction**

43 Earthen flood defence embankments also known as levees are long structures usually made of
44 local material available at the construction site. In the UK, flood defence embankments are
45 mainly made of cohesive soils: either clay or silt. Most of them were built before the
46 development of modern soil mechanics in the eighteenth century (Charles, 2008). Due to
47 their progressive aging, proper infrastructure condition assessment, based on sound
48 engineering, is becoming increasingly important (Perry et al., 2001).

49 The formation of desiccation cracks in earthen embankments and tailing dams
50 (Rodriguez et al., 2007) made of cohesive soils during dry seasons is detrimental to their
51 stability. Desiccation is responsible for the onset of primary cracks which first appear at the
52 surface, and then propagate downwards, and for so-called secondary and tertiary cracks
53 (Konrad and Ayad, 1997). Desiccation induced failures are deemed to become increasingly
54 important as progressively more extreme weather conditions are predicted by climatologists
55 to take place worldwide (Milly et al, 2002). Allsop et al. (2007) provide a comprehensive list
56 of the several failure modes that may take place in earthen embankments. Several potential
57 failure mechanisms are negatively affected by the presence of desiccation cracks such as:
58 deep rotational slides starting from the horizontal upper surface (Utili, 2013); shallow slides
59 developing along the flanks (Aubeny and Lytton 2004; Zhang et al., 2005); erosion of the
60 flanks by overtopping water (Wu et al., 2011) and/or wave action (D’Elisio, 2007); and
61 internal erosion (Wan and Fell, 2004). In particular, the presence of cracks can substantially
62 decrease the resistance of embankments with regard to overtopping and internal erosion
63 which alone count for 34 and 28 percent respectively of all the embankment failures in the
64 world (Wu et al., 2011).

65 Monitoring and condition assessment of flood defence embankments worldwide are
66 mainly carried out by visual inspections at set intervals (Morris et al., 2007; Andersen et al.,

67 1999). In a few countries (e.g. the UK (Environment Agency, 2006), the Netherlands, the US)
68 guidelines exist to rate the health/deterioration of embankments on the basis of a prescribed
69 set of visual features. Unfortunately, this type of assessment is purely qualitative and relies
70 heavily on the level of training and experience of the inspection engineer. So, there is
71 consensus among experts on the fact that although visual inspection provides valuable
72 information, a meaningful and robust assessment of the fitness for purpose of earthen flood
73 defence embankments cannot rely entirely on visual inspection (Allsop et al., 2007). On the
74 other hand, intrusive tests (e.g. Cone Penetration test, piezocones, vane tests, inclinometers)
75 are impractical for the monitoring of long structures like embankments given the necessity of
76 performing tests in several locations to account for the typical high variability of the ground
77 properties. The same applies to standard geotechnical laboratory tests which involve time-
78 consuming retrieval and transportation of samples to the laboratory.

79 In this paper, a cost effective approach employing a suite of geotechnical and geophysical
80 probes is proposed for the long term monitoring of the variation of water content in the
81 ground and of the liability to desiccation induced fissuring. The methodology is simple,
82 modular (*i.e.* the level of sophistication/accuracy is a function of the financial resources
83 available), and it can be readily implemented by the authorities in charge of the management
84 of earthen flood defence embankments and tailing dams.

85

86 **2. Conceptual framework**

87 The methodology here proposed is based on the assumption that water content can be
88 selected as a direct indicator of the occurrence of extensive fissuring in the ground as
89 suggested by Dyer et al., (2009) and Tang et al., (2012). The authors are aware that a lot of
90 research has been recently performed to successfully relate the onset of cracks to soil suction
91 (e.g. Shin and Santamarina, 2011; Munoz-Castelblanco et al., 2012b). However, as recently

92 well illustrated by Costa et al., (2013), the formation and propagation of cracks in cohesive
93 soils depends on several other factors too, such as the drying rate and the amount of fracture
94 energy involved in the crack propagation. Considering flood defence embankments, loss of
95 structural integrity (*i.e.* loss of the structure capacity to withstand the design hydraulic load)
96 occurs when desiccation fissuring progresses to the extent that an interconnected network of
97 cracks is formed rather than when surficial cracks first appear. Therefore the approximation
98 introduced in relating the loss of structural integrity to a threshold value of suction appears no
99 less important than the approximation introduced in relating it to a threshold value in terms of
100 water content. Moreover, the cost of monitoring suction in a long embankment for an
101 extended period of time is very significant with the extra burden of necessitating complex
102 installation and maintenance procedures for the probes needed to measure suction. These
103 reasons underpin the authors' choice of monitoring the ground water content.

104 The position of any point in a long linear structure like an embankment or tailing dam
105 can be defined according to either a global Cartesian coordinate system (X,Y,Z) or a local
106 coordinate system defined at the level of the structure cross-sections. For sake of simplicity,
107 the following choice was made: a curvilinear global coordinate, s , running along the
108 longitudinal direction of the structure which uniquely identifies the location of any cross
109 section; a local Cartesian coordinate, x , lying in the horizontal plane and perpendicular to the
110 s coordinate; and a vertical downward Cartesian coordinate, z , which can be thought of as
111 both a global and local coordinate. So, the water content, w , in a generic point of the earthen
112 structure is a function of these three spatial coordinates and of time: $w(x,s,z,t)$. A local
113 tangential coordinate s_t was also defined as shown in Figure 1b. The procedure proposed to
114 determine the function $w=w(x,s,z,t)$ in the whole embankment is based on the following
115 actions:

- 116 1) measurement of the water content profile along a vertical line P of coordinate x_p, s_p at
117 any time and depth $w(x = x_p, s = s_p, z, t) = w_p(z, t)$;
- 118 2) measurements in some selected cross-sections, located at $s = s_i$ (herein the subscript i
119 is an integer identifying the embankment cross-section considered), at some discrete
120 time points t_k (herein the subscript k is an integer identifying the time point
121 considered), of the function $w(x, s = s_i, z, t = t_k) = w_{i,k}(x, z)$;
- 122 3) measurement by geophysical techniques of the water content at predefined time
123 points, t_k , along the entire embankment (*i.e.* for any value of s);
- 124 4) evaluation by extrapolation of the water content in any point at any time: $w(x, s, z, t)$.

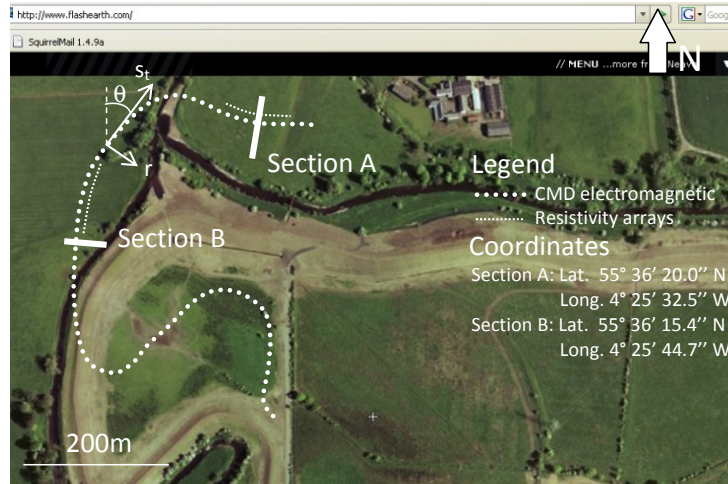
125 Once the water content function $w(x, s, z, t)$ is determined, an index quantifying the
126 susceptibility of any cross-section of the embankment to desiccation fissuring can be defined
127 and a map of susceptibility can be generated to identify the most critical zones of the
128 structure (see section 8). The map is useful to set priorities for intervention in the zones
129 requiring remedial actions.

130

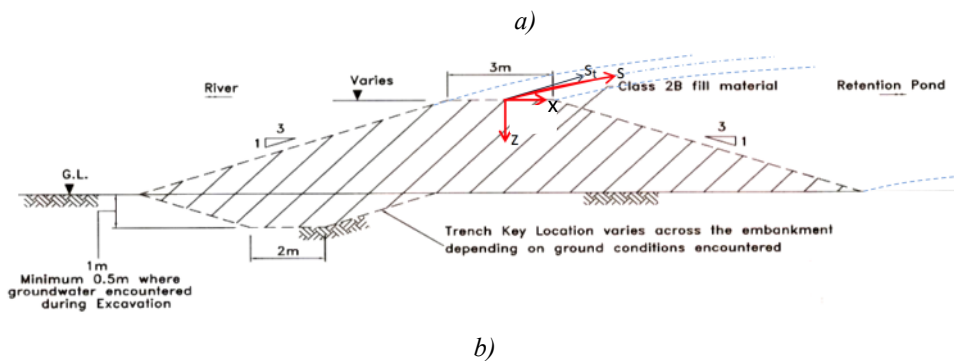
131 **3. Description of the site**

132 In 2007, the construction of an earthen flood defence embankment enclosing a floodplain
133 along the river Irvine to drain excess waters from the river during floods was completed in
134 Galston (Scotland, UK). The embankment is made of an uppermost layer (5-10 cm) of a
135 sandy topsoil below which lies a core of glacial till containing several boulders (Figure 1).
136 Grass roots do not extend beyond the topsoil. A typical cross- section is sketched in Figure
137 1b. Although the inclination of the flanks is rather uniform, the size of the flanks and of the
138 upper surface vary quite substantially along the longitudinal direction giving rise to a non-

139 negligible spatial variation of the geometry of the cross-sections which may have
 140 consequences in terms of the spatial variation of the water content in the ground (see sections
 141 6 and 7).



142
 143



144
 145

146 *Figure 1. a) Plan view of the monitored embankment; b) typical embankment cross section and system of*
 147 *coordinates adopted in the paper.*

148

149 A number of standard geotechnical tests were carried out to characterise the ground
 150 properties: measurements of gravimetric moisture content, void ratio, particle size
 151 distribution and Atterberg limits were taken. The grain size distribution of both the top soil
 152 and the glacial till was determined according to ASTM E11 (see Figure 2).

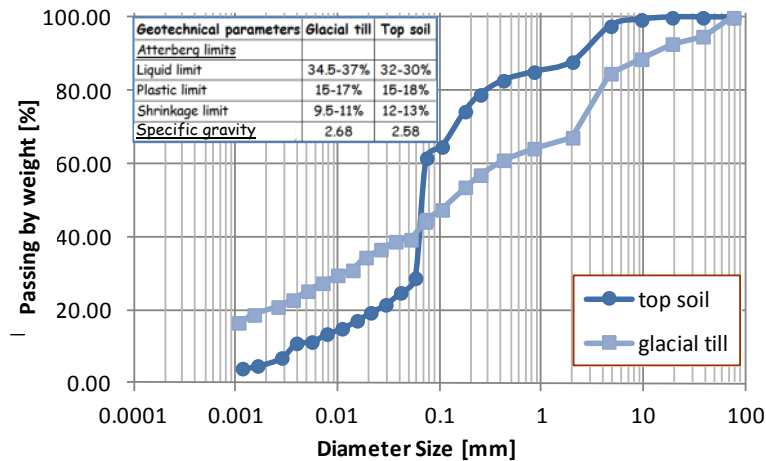


Figure 2. Particle size distribution of the glacial till and of the topsoil and main geotechnical indices.

4. Monitoring system

In the following, the main geotechnical and geophysical measurements of the monitoring system are described. The main technical features of all the probes employed in the monitoring programme (e.g. manufacturer, accuracy, operational range, etc.) are listed in Table 1.

4.1 Measurement of the water content along the selected vertical P

In Figure 3b, the vertical line P is plotted with the label PR2_E2. A data-logger, reading data at an hourly frequency was installed into a bespoke metallic fence close to the vertical line P (see Figure 3c). As schematically shown in Figure 3a and b, the following devices were connected to the data-logger:

- a) a theta probe (THP) made of four metal rods to be inserted in the ground to measure its water content at a depth of 25 cm. Special care was taken to avoid the formation of any air gaps between the prongs of the probe and the surrounding soil by prefilling the augered holes hosting the probes with a slurry and pushing the probe into undisturbed soil well beyond the hole bottom. The device takes a measurement of the relative

- 172 permittivity (also commonly called dielectric constant) of the ground which is then
173 converted into gravimetric water content;
- 174 b) an equitensiometer (EQ) to measure suction up to a maximum value of 1000 kPa at
175 the same depth of 25 cm. This device consists of theta probe pins embedded into a
176 porous matric;
- 177 c) a portable profile probe (PR), which is based on time domain reflectometry, to
178 measure the water content at six different depths from the ground surface (10, 20, 30,
179 40, 60 and 100 cm);
- 180 d) two temperature probes inserted at 25 and 40 cm of depth in the ground.

181

182 **4.2 Measurement of the water content at cross-section A and B**

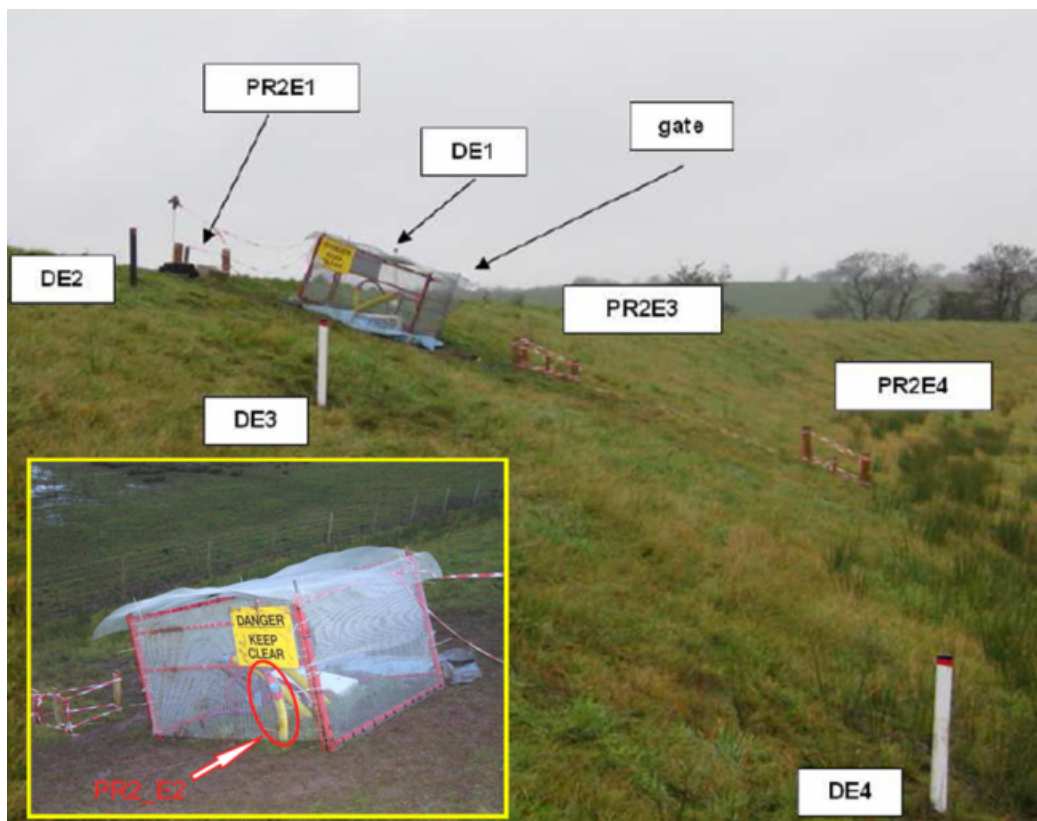
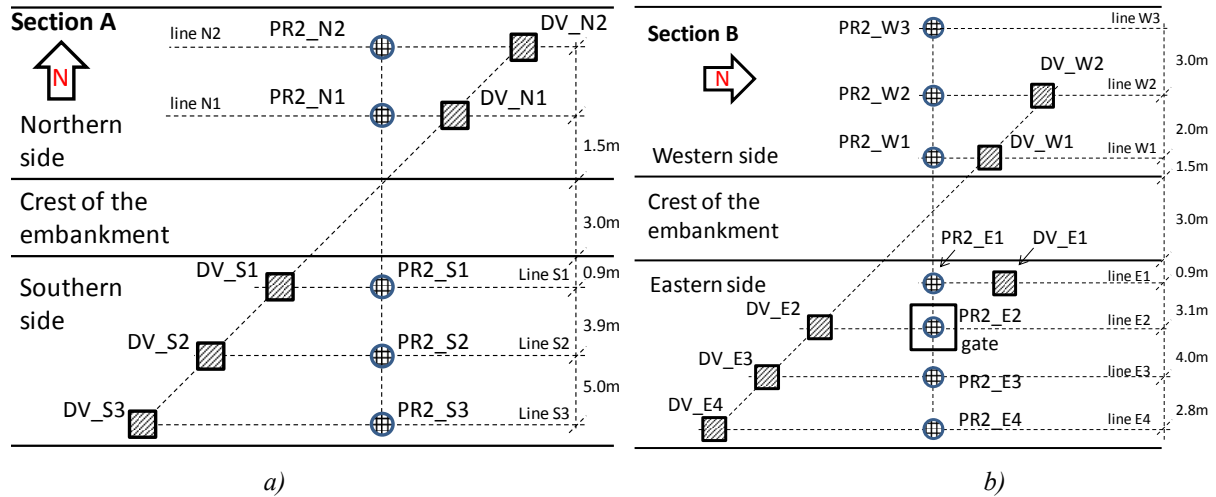
183 To evaluate the water content in the ground up to 1 meter of depth, several access tubes were
184 drilled into two cross-sections (A and B in Figure 3a and b) with the property of being
185 perpendicular to each other to better account for the influence of topographical orientation on
186 the measured water content (see section 7). Special care was taken to avoid the formation of
187 any air gaps between the tubes where the PR was inserted and the surrounding soil. Two
188 different instruments were employed:

- 189 a) the PR, already described in the previous section, to measure the ground water content
190 along several vertical lines up to a depth of 1 m;
- 191 b) a portable diviner (D) (see Sentek Diviner 2000 in table 1) to measure the ground
192 water content along various vertical lines every 10 cm from ground level down to 1.6
193 m of depth. This device is based on frequency domain reflectometry.

194 In section A, 10 access tubes were employed: 5 for the profile probe (labeled PR2_xx)
195 and 5 for the diviner (labeled DV_xx). In section B there were 12 measuring points: 6 for the
196 profile probe and 6 for the diviner. Some of the access tubes for the profile probe and the

197 diviner were laid down so as to be aligned along the longitudinal direction of the
 198 embankment in order to perform a cross-comparison between them as it will be illustrated in
 199 section 5 (see Figure 3a and b).

200
 201
 202



203
 204
 205
 206
 207

c)
 Figure 3. Position of the access tubes for the profile probe (PR2) and the diviner (D): (a-b) plan view of sections A and B, respectively; (c) view of cross section B from the Eastern side.

208 A weather station, manufactured by Pessl Instruments (see table 1), was installed 200m
 209 south from section B of the embankment in order to collect data on rainfall precipitation, air
 210 humidity, temperature and wind speed over the two year period of monitoring.

211

212 *Table 1. Main technical features of the probes employed in the monitoring.*

Device	Product name	Manufacturer	Accuracy and operational range
Equitensiometer	EQ2	Delta-T Devices Ltd United Kingdom www.delta-t.co.uk/	±10 kPa in the range from 0 to -100 kPa, ±5% in the range from -100 to -1000 kPa.
Theta probe	THP	Delta-T Devices Ltd United Kingdom www.delta-t.co.uk/	after calibration to a specific soil type: ±0.01 m ³ .m ⁻³ , in the range from 0 to 0.4 m ³ .m ⁻³ with temperature from -20 to 40°C,
Profile probe	PR2	Delta-T Devices Ltd United Kingdom www.delta-t.co.uk/	after calibration to a specific soil type: ± 0.04 m ³ .m ⁻³ , in the range 0 to 0.4 m ³ .m ⁻³ reduced accuracy from 0.4 to 1 m ³ .m ⁻³
Diviner	Diviner 2000	Sentek Pty Ltd Australia www.sentek.com.au	+/- 0.003% vol in the range from -20 to +75°C
Weather station	iMETOS pro	Pessl Instruments http://metos.at/joomla/page/	temperature: +/- 0.1°C in the range -40° to +60° relative humidity: 1 % in the range 0 to 100% wind speed: 0.3 m/s in the range 0 to 60 m/s precipitation: +/- 0.1mm
Electromagnetic probe	CMD-2	Gf Instruments Czech Republic http://www.gfinstruments.cz	± 4% at 50 mS/m Operating temperature: -10 °C to +50 °C Maximum sampling rate: 10 Hz

213

214 4.3 Geophysical measurements

215 Electromagnetic surveys present the advantage of being non-intrusive and quick to be carried
 216 out. Electromagnetic probes can measure the electrical conductivity of the ground. The
 217 CMD-2 probe from Gf Instruments (see Table 1) was chosen for being a relatively cheap
 218 device and simple to be used, *i.e.* without requiring a specific training. In Gf Instruments
 219 (2011) the working principles of the device are illustrated. Measurements were taken by an
 220 operator walking on the horizontal upper surface of the embankment along the longitudinal
 221 direction at a constant pace of 5km/h, holding the CMD-2 approximately 1m above ground
 222 with the device oriented perpendicular to the longitudinal direction so that the
 223 electromagnetic flow-lines always lie in the plane perpendicular to the longitudinal direction
 224 (*i.e.* the plane of the embankment cross-section).

225 Electrical resistivity tomography (ERT) is also a well-established geophysical technique
226 that is increasingly employed to measure electrical conductivity at the ground surface
227 (Munoz-Castelblanco et al., 2012a). Nowadays, 3D maps of in-situ water content can be
228 generated from ground resistivity measurements, as shown in (De Vita et al., 2012; Di Maio
229 and Piegari, 2011), once appropriate correlations between ground resistivity and in-situ water
230 content have been established. The potential for obtaining 3D maps of water content makes
231 ERT look like a very attractive tool for the monitoring of embankments. However, ERT
232 appears to be impractical for the continuous monitoring of an extended structure over long
233 timespans since it requires operators possessing the specialist skills to install the electrodes of
234 the devices in the ground and operate them. For this reason, in order to take geophysical
235 measurements of electrical conductivity in the embankment (see section 7.2) we chose to use
236 electromagnetic probes instead. Nevertheless, in the authors' opinion, ERT could still be
237 beneficially employed in the zones of the embankment identified as critical by the integrated
238 geotechnical/geophysical approach here proposed. In fact, ERT is useful to investigate in
239 great detail the state of fissuring of the ground in zones of limited extent.

240

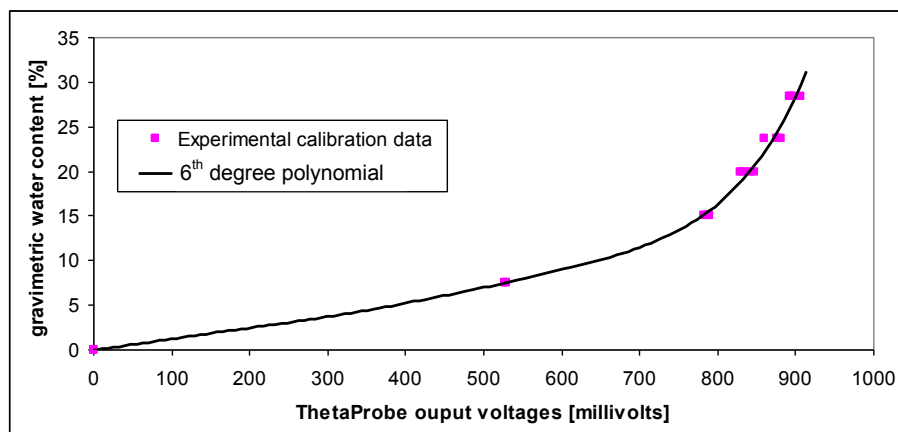
241 **5. Calibration of the geotechnical suite**

242 A key point of any monitoring system is the proper calibration of all the employed devices.
243 Regarding the calibration exercise undertaken, only the glacial till is of interest since the
244 thickness of the top soil in the embankment flanks, where all the measurements were taken, is
245 5 cm and the measurements were taken at depths always larger than 10 cm. A sequential
246 approach was adopted which is detailed in the following.

247

248 **5.1 Direct calibration of the theta probe**

249 The calibration curve for the theta probe (THP) was taken from Zielinski, (2009) (see Figure
250 4) who calibrated the THP using samples of till retrieved from the same quarry (Hallyards,
251 Scotland, UK) from which the till of our monitored embankment was extracted. The till was
252 retrieved from the quarry at five different known water contents and compacted into five
253 cylindrical containers with the same compaction effort as in the monitored embankment, *i.e.*
254 relative compaction of 95% with compaction control performed according to the
255 *Specification for Highway Works: Earthworks, Series 6000* (Highways Agency, 2006). Given
256 the high level of compaction and the non-swelling nature of this glacial till, the variations of
257 dry unit weight in the embankment over time and space occurring for the range of measured
258 in-situ water contents can be considered negligible (less than +/-5%). Hence, we transformed
259 the volumetric water contents measured by the geotechnical probes (profile probe, diviner,
260 etc.) into gravimetric water contents assuming the dry unit weight of the till at its optimal
261 water content, *i.e.* a maximum dry unit weight of 19.1 kN/m³. This value was obtained as
262 average of 7 measurements performed in the laboratory on undisturbed U-38 samples
263 retrieved from the embankment. This value turned out to be almost identical to the value
264 measured by (Zielinski, 2011) on a small scale embankment built from the same glacial till
265 reconstituted in the laboratory.



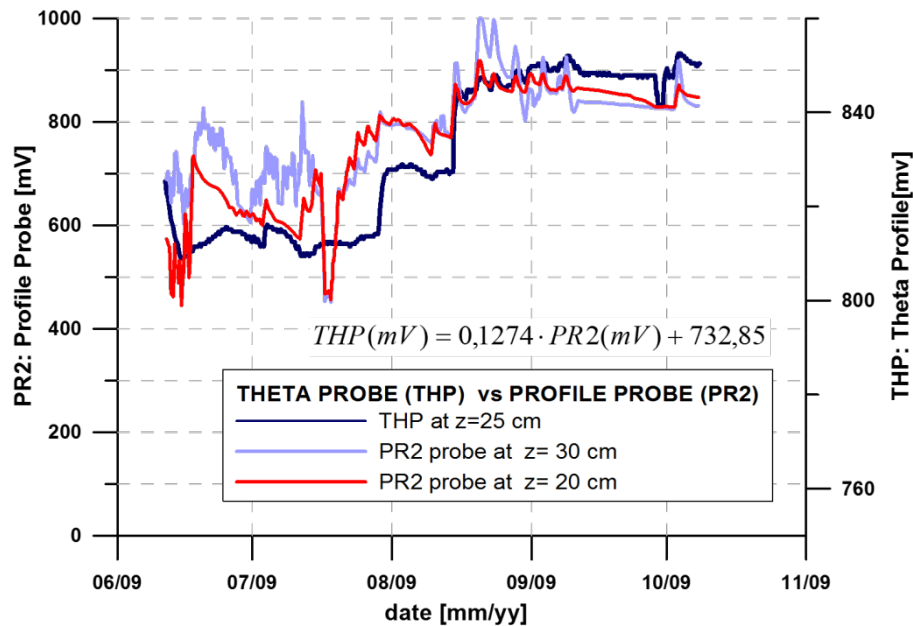
266
267 *Figure 4. Calibration curve for the theta probe; experimental calibration data after Zielinski (2009).*

268

269 **5.2 Indirect calibration of the profile probe**

270 The calibration of the profile probe (PR) was obtained by comparing the raw data in
271 millivolts obtained by the PR located at the gate in section B (PR2_E2 in Figure 3) at 20 and
272 30 cm depth with the measurements of the theta probe (THP) in the same location (20 cm
273 longitudinally away from the PR2_E2 in Figure 3) at 25 cm depth for a 4 month period. Data
274 were recorded every 4 hours. A strong similarity between the trends of the readings of the
275 two probes plotted in Figure 5 was observed. Since the two devices measure the water
276 content of the same portion of soil, a calibration procedure, based on the visual match of the
277 curves, was adopted: the scale of the ordinate axis of the THP readings (expressed in mV)
278 was varied until it satisfactorily matched the average (not reported in the figure to avoid
279 cluttering) of the two measurements at 20 and 30 cm depth obtained by the THP. The
280 resulting linear relationship between the values measured by the PR and the values measured
281 by the THP is shown in Figure 5. This relationship was used to convert the readings of the PR
282 into equivalent milliVolt units measured by the THP, and then they were in turn transformed
283 into gravimetric water content employing the calibration curve of the THP (Figure 4).

284



285

286 *Figure 5. Calibration of the profile probe: measurements by the theta probe and the profile probe taken at the*
 287 *same location, PR2_E2 (see Figure 3).*

288

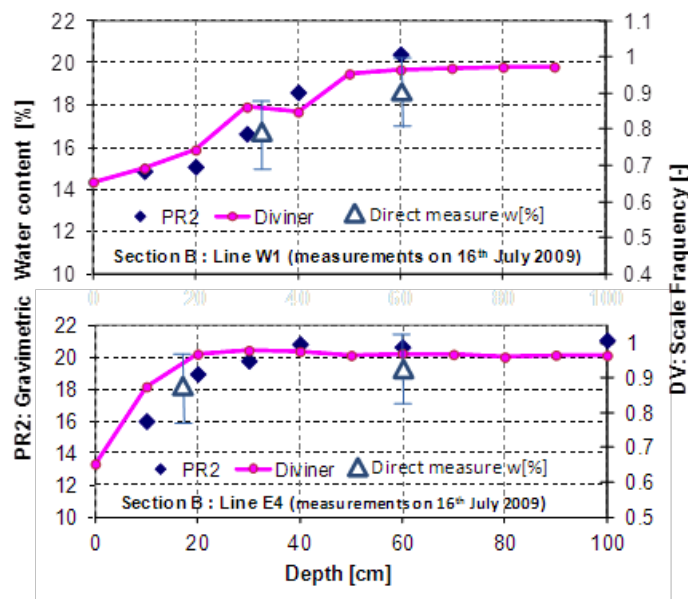
289 **5.3 Indirect calibration of the diviner**

290 Following the same approach described in the previous section, indirect calibration of the
 291 diviner (D) was performed by varying the scale of the frequencies measured by the D until a
 292 satisfactory match with the water content profile measured by the PR in the corresponding
 293 access tube was obtained. The corresponding PR access tube is the one aligned with the D
 294 tube in the longitudinal direction (e.g. DV_S3 and PR2_S3, see Figure 3a). In Figure 6a, two
 295 of the performed calibrations are shown. The curve shown in Figure 6b was obtained by
 296 repeating this procedure for all the monitoring points of the D in the time period considered.

297 Since the calibration procedures adopted for the PR and the D are based on cross-
 298 correlation, errors of measurement could be amplified. Hence, in order to check the amount
 299 of error amplification, direct measurements of the gravimetric water content were obtained
 300 via small in-situ samples taken in several points of the embankment on the same day (see the
 301 triangles in Figure 6a). Looking at Figure 6a, a good agreement between the values of water

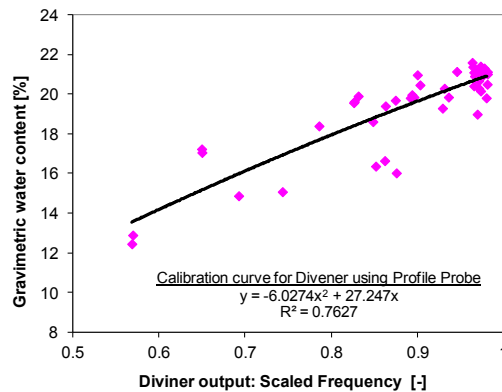
302 content measured by the indirectly calibrated probes (PR and D) and direct measurements
 303 emerges so that it can be concluded that error propagation is within acceptable limits.

304 Overall, the adopted calibration procedure has the obvious advantage of requiring only
 305 small samples of soil for the direct calibration of the THP in the laboratory with the PR and D
 306 indirectly calibrated in-situ. Conversely, direct calibration of the PR and D would require
 307 retrieving large volumes of soil, to avoid the influence of boundary effects, at predefined
 308 water contents to the laboratory.



309
 310

a)



311
 312

b)

313 *Figure 6. Calibration of the diviner by comparison with the measurements of the profile probe: a) examples of*
 314 *cross comparisons for measurements taken in access tubes lying along the longitudinal line W1 and E4 (see Fig.*
 315 *3 for location of the lines). The triangles with their error bar indicate the values of water content obtained via*
 316 *direct measurement. b) Obtained calibration curve for the diviner.*

317

318 **6. Monitored data**

319 In this section data relative to rainfalls, wind speed, relative humidity, air and ground
320 temperature recorded by the weather station installed near to the embankment are analysed
321 and compared with the ground water content recorded by the geotechnical suite in cross-
322 sections A and B. The purpose of this analysis was first to establish the variation in time and
323 space of the water content and secondly to identify correlations between weather variables
324 and ground water content in order to separate out the variables significantly affecting the
325 water content from the ones with a marginal influence which therefore can be discarded from
326 the monitoring programme.

327 In principle it would be possible to calculate the effective amount of rainfall infiltrating
328 in the ground from the calculation of evapotranspiration rates and the measurement or
329 calculation of the amount of water runoff (Smethurst et al., 2012; Xu and Sing, 2001).
330 However, the amount of runoff is likely to depend strongly on the inclination of the
331 embankment flanks which varies locally and to a lesser extent on to the local vegetation
332 cover. Moreover, a reliable estimate for a long linear structure with varying cross-section
333 geometries would require several points of measurement. This is against the overall
334 philosophy of the proposed methodology which aims to be as practical and simple as
335 possible. Hence, we sought a relationship between in-situ water content and total precipitated
336 rainfall. The latter can be measured directly by a nearby weather station. Furthermore, in the
337 UK at least, weather stations can be found in several localities so that often there will be no
338 need to install a new station in the site of interest. In summary, on one hand using total
339 rainfall makes the correlation with the in-situ water content weaker because of the extra
340 approximation of disregarding the variation of effective rainfall in the ground due to local
341 lithological and geometrical variations; however on the other hand, it is far more desirable for

342 the authorities in charge of the monitoring system since total rainfall is much easier to be
343 ascertained.

344

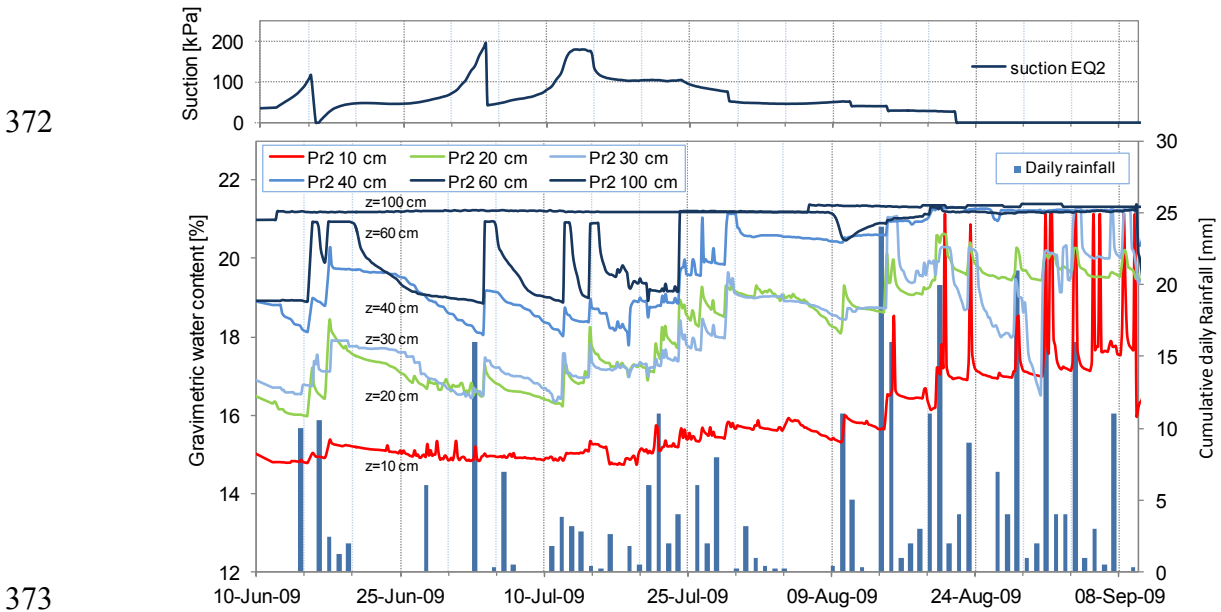
345 **6.1 Continuous measurements of water content profiles**

346 Data were recorded over a 2 year period. Here, only an extract of two significant periods is
347 provided to illustrate the seasonal trends of desiccation and wetting of the embankment. The
348 most significant seasons are summer (see Figure 7) and winter (see Figure 9). In Figure 7a,
349 the ground water content profile is plotted together with the recorded daily rainfall
350 precipitation. Precipitations larger than about 5mm/day or reaching 5mm over a period of
351 consecutive daily rainfalls lead to noticeable increases of water content apparent in the spikes
352 of the curves relative to the water contents measured at 10 and 20 cm depth. No significant
353 variations of water content were ever recorded at depths larger than 60 cm.

354 In the upper part of Figure 7a, the suction measured by the EQ2 at 25 cm depth is
355 plotted. It emerges that the suction is well related to the rainfall records as well as to the
356 variation of water content. After several consecutive days of rainfall in late August, the
357 suction vanished to 0 for the entire winter period. For this reason, the variation of suction was
358 not reported in Figure 9b relative to the winter period. The THP measured water content at
359 the same depth of the suction measurements of the EQ in a point 15 cm away along the
360 horizontal direction so that an in-situ suction-water characteristic curve (SWCC) for the
361 considered point (PR2_E2) can be obtained (curve C in Figure 8). Zielienski et al. (2011)
362 measured in the laboratory the SWCC of this glacial till with different techniques (curves A
363 in Figure 8) and the SWCC (curve B in Figure 8) in a small scale embankment made of the
364 same material. In Figure 8, all these curves are plotted. Comparing the curves, it emerges that
365 the values of in-situ suction measured by the EQ lie close to the SWCC curves obtained in

366 the laboratory and also that the boundaries of the hysteresis cycles are close. This result is
367 quite remarkable.

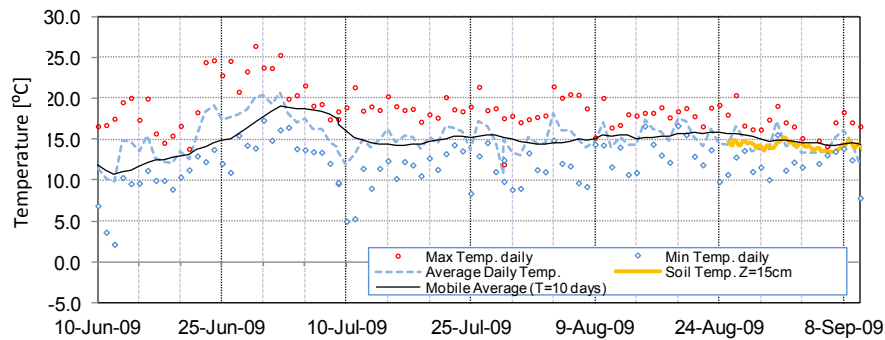
368 Examining the recorded temperatures of the air and ground, a clear correlation between
369 the two is found: in Figure 7b the average between the maximum and minimum daily air
370 temperature turns out to be very close to the ground temperature at 10 cm depth. Relative
371 humidity and wind speed were rather constant during the monitored period (see Figure 7c).



373

374

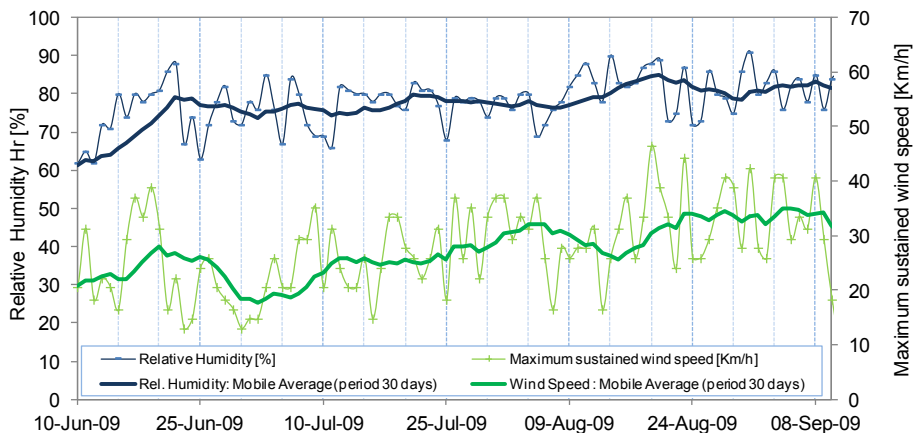
a)



375

376

b)



377

378

c)

379

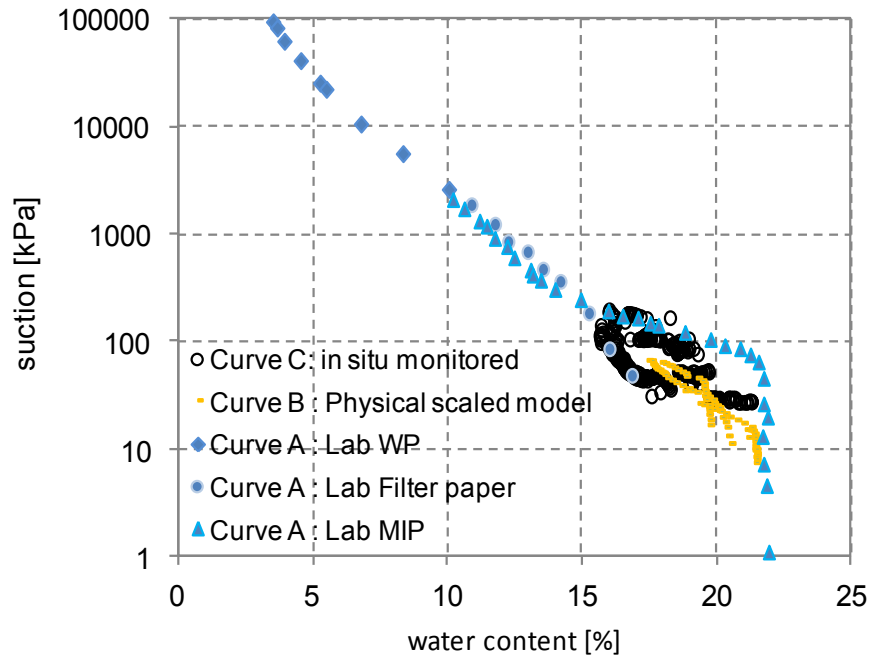
380

381

382

383

Figure 7. Summer 2009 (section B): a) evolution of the gravimetric water content, suction and rainfall record; b) average between the maximum and minimum daily air temperature (grey line) and ground temperature measured at 10cm depth; c) relative humidity and wind speed: the thin line follows the daily variation whereas the thick line is the mobile average over 10 days.



384

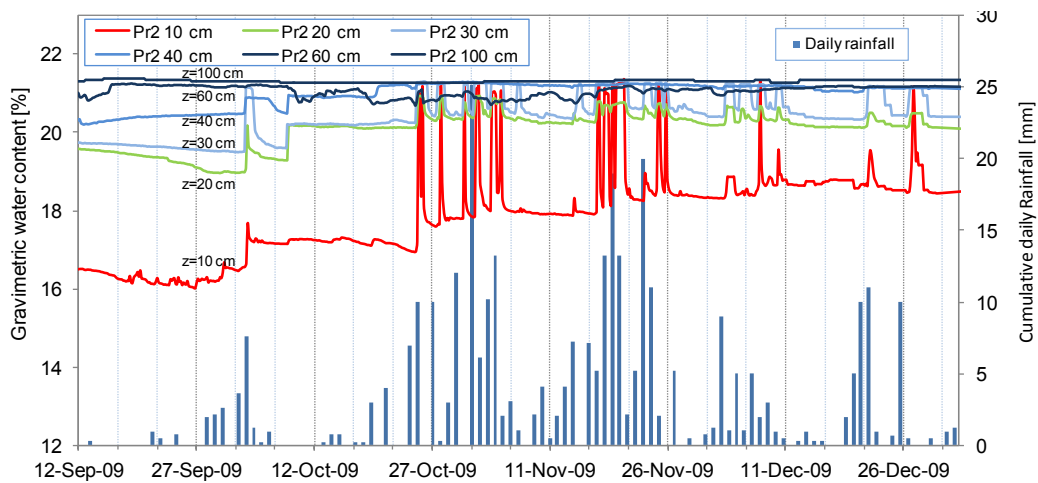
385 *Figure 8. Comparison of in situ suction - water characteristic curve (SWCC) derived from measurements taken*
 386 *by the THP and the EQ at 25 cm depth (Curve C) with the SWCC determined from reconstituted samples*
 387 *(Curves A, after Zielinski et al. (2011)) and in a small scale embankment model (Curve B, Zielinski et al.*
 388 *(2011)).*

389

390 In winter (see Figure 9), higher precipitations take place leading to significantly larger
 391 quick increases of the ground water content, in particular at shallow depths (10 cm). The
 392 same remarks as for the summer period can be made with the exception of the wind speed
 393 which varies significantly more than during the summer period.

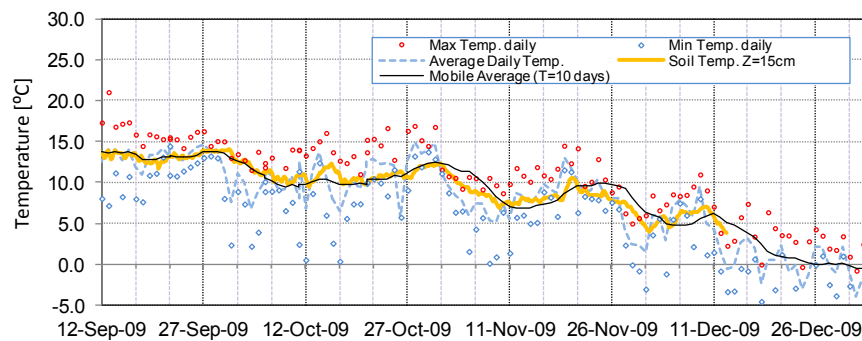
394 From the monitored data, it can be concluded that the ground water content is highly
 395 sensitive to the amount of total precipitation and to the length of the dry periods whereas no
 396 significant correlation to relative humidity or to the variation of wind speed was found. These
 397 observations lead to state that in principle it is possible to estimate the water content in a
 398 cross-section, and in turn the cross-section susceptibility to desiccation fissuring (see section
 399 8), from knowledge of both ground water content at the initial time of monitoring and
 400 historical rainfall records. Given the limited resources available in this project, continuous
 401 measurements in time are available only in 1 section of the embankment which is too little to
 402 validate a reliable correlation between historical rainfall records and water content. However

403 in light of the results obtained here, we suggest that if a sufficient number of sections are
 404 instrumented, a reliable correlation may be established so that meteorological data (especially
 405 rainfall records) could be used to infer the amount of water content along the entire
 406 embankment at any time according to the methodology presented in the next section (section
 407 7) and to monitor susceptibility of the structure to desiccation fissuring (as expounded in
 408 section 8). This methodology would have the advantage of not requiring periodic walk-over
 409 surveys, but only the presence of a weather station nearby the structure.
 410



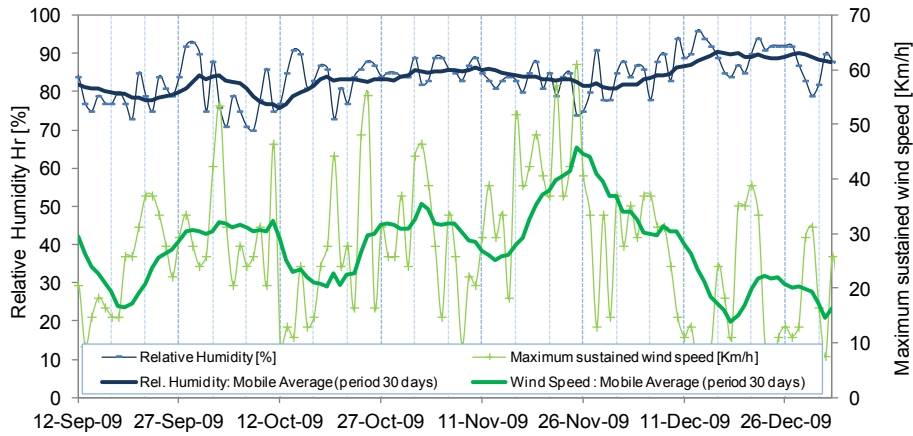
411
 412

a)



413
 414

b)



415

416

c)

417

Figure 9. Winter 2009 (cross-section B): a) evolution of the gravimetric water content and rainfall record; b)

418

average between the maximum and minimum daily air temperature (grey line) and ground temperature

419

measured at 10cm depth; c) relative humidity and wind speed: the thin line follows the daily variation whereas

420

the thick line is the mobile average over 10 days.

421

422

6.2 Time discrete measurements of water content profiles

423

To evaluate $w_{i,k} = w(x, z) = w(x, s = s_i, z, t = t_k)$, measurements were taken from the profile

424

probe (PR) and the diviner (D) up to a depth of 1m (see Figure 10). In Figure 11a and Figure

425

11b, the evolution of the water content over time is plotted for section A and B respectively.

426

These figures were obtained by interpolating in space the values of water content measured

427

from the locations of the monitoring points (see Figure 3). The analyzed domain consists of

428

the uppermost 1 m of the cross-sections since no significant variations of water content were

429

ever observed at larger depths (see Figure 7 and Figure 9). To generate the plotted contours

430

of water content, first a mesh was created whose nodes coincide with the locations of the

431

readings taken from the PR and the D, then a post-processing FEM software, called GID

432

(GID, 2014), was employed to interpolate the values along the x and z coordinates. The

433

interpolation was repeated for measurements taken at different times (see Figure 11). From

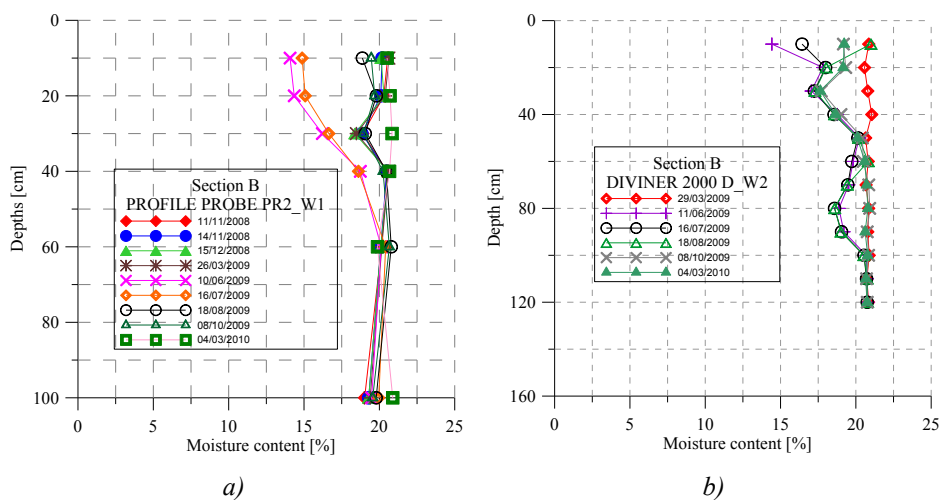
434

these data it emerges that the water content varies significantly between the two sections. The

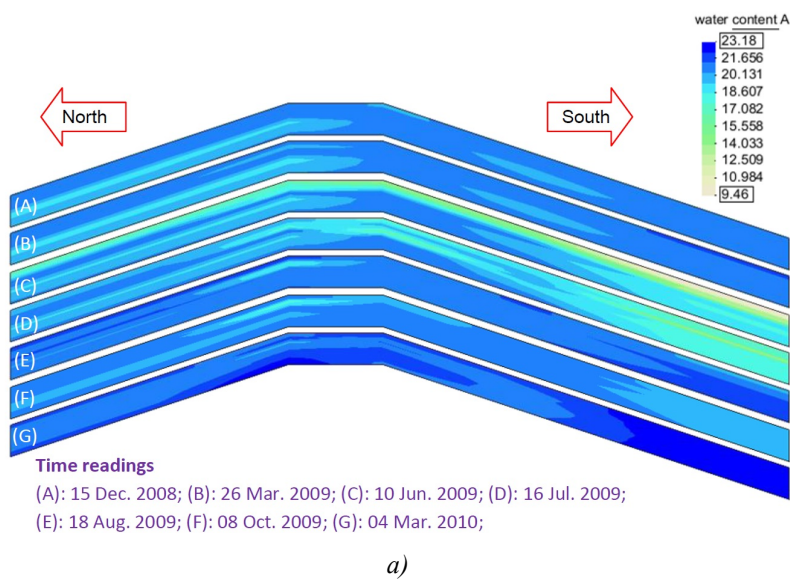
435

dependence of the water content on the geometrical alignment of the cross-sections, has been

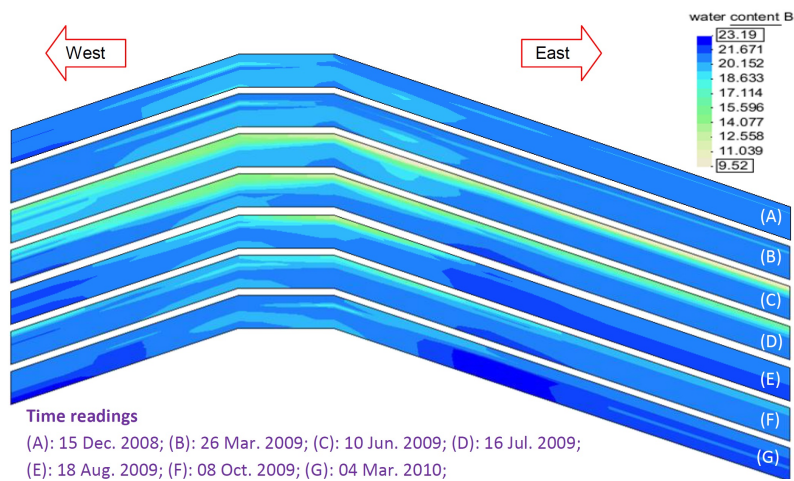
436 accounted for in deriving the function $w(x,s,z,t)$ as it will be illustrated in the next
 437 paragraph.



438
 439
 440 *Figure 10. Examples of profiles of the water content at different times in cross-section B: a) obtained by the*
 441 *profile probe; b) obtained by the diviner.*



442
 443



444

445

b)

446 *Figure 11. Contours of the water content at different times over a period of 1.5 years: a) in cross-section A; b)*
447 *in cross-section B.*

448

449 **7. Extrapolation of the water content function for the entire structure**

450 In the following, $w(x,s,z,t)$ will be derived first on the basis of data gathered by the
451 geotechnical suite only, secondly employing measurements of electrical conductivity taken
452 by the CMD-2 probe as well.

453

454 **7.1 Derivation of the water content function from the data retrieved by the geotechnical** 455 **suite**

456 In Figure 11, the water content of the two monitored cross-sections (A and B) is plotted. The
457 water content in any other cross-section is different due to two main factors:

- 458 (i) different exposure to weather conditions (e.g. sunlight, rainfall and wind) which is a
459 function of the local orientation of the considered cross-section with respect to North.
460 This factor affects the ground water content along the flanks of the embankment much
461 more than underneath the horizontal upper surface.
- 462 (ii) spatial variation of the geometrical, hydraulic and lithological properties of the cross
463 sections along the longitudinal coordinate s . Heterogeneities in the compaction
464 processes during construction, for example, are likely to cause a non-negligible spatial
465 variation of the hydraulic conductivity along the longitudinal direction. Concerning
466 compositional or lithological variability, this is likely to be small for the embankment
467 examined here due to the fact that it is made of homogeneous material and its young
468 age. However, in general, old earthen embankments are very often highly
469 heterogeneous comprising a mixture of several materials locally available at the time
470 of construction.

471 Regarding factor (i), considering the axis of symmetry of the cross-section (axis z in Figure
472 1a), exposure to each single weather element (e.g. wind, sunrays, rainfall droplets, etc.) gives
473 rise to a variation of water content which is either anti-symmetrical or nil in the case of equal
474 exposure (e.g. no wind and vertical sunrays), but the combination of the single weather
475 elements, *i.e.* the sum of the anti-symmetrical variations of water content due to exposure to
476 wind, exposure to sunrays, etc., may give rise to a non-negligible symmetrical variation of
477 water content as well. The anti-symmetrical part is a function of the orientation of the cross-
478 section considered whereas the symmetrical one is a function of the longitudinal coordinate s .
479 Regarding factor (ii), geometrical, hydraulic and lithological variations in the embankment
480 imply a variation of water content which in authors' opinion is much larger along the
481 longitudinal coordinate s than within each single cross-section and therefore is mainly
482 symmetrical. In summary, the water content variation in the embankment depends on both
483 cross-section orientation and cross-section position. The latter is expressed by the
484 longitudinal distance from a reference cross section (coordinate s). To better account for the
485 variation of water content due to these geometrical factors, cross-section orientation and
486 cross-section position, it is convenient to split the water content function, $w(x, s, z, t)$, into two
487 parts, a symmetrical, w^s , and an anti-symmetrical one, w^a , with respect to the axis of
488 symmetry of the cross-section:

$$489 \quad w^s(x, s, z, t) = \frac{w(x, s, z, t) + w(-x, s, z, t)}{2} \quad \text{and} \quad w^a(x, s, z, t) = \frac{w(x, s, z, t) - w(-x, s, z, t)}{2} \quad (1)$$

490 To account for the influence of cross-section orientation, it is convenient to employ a
491 function $\theta(s)$, with θ being the angle between s_t , direction normal to the cross-section, and a
492 reference direction here chosen as the geographical North (see Figure 12a). Considering
493 measurements of water content at discrete time points t_k , $w_k^a(x, s, z) = w^a(x, s, z, t = t_k)$ can be

494 expressed as the weighted average of the values of water content,

495 $w_{i;k}^a(x, z) = w^a(x, s = s_i, z, t = t_k)$, recorded at $t = t_k$ in the N instrumented cross-sections:

496
$$w_k^a(x, s, z) = w^a(x, s, z, t = t_k) = \sum_{i=1}^N w_{i;k}^a(x, z) \cdot \alpha_i(\theta) \quad (2).$$

497 with $\alpha_i(\theta)$ being weight functions accounting for the anti-symmetrical water content

498 variation in the embankment. The simplest choice for $\alpha_i(\theta)$ is to consider a linear

499 interpolation between the values of water content measured at the N instrumented sections as

500 illustrated in Figure 12c, so that:

501
$$\alpha_i(\theta) = \begin{cases} 1 & \text{for } \theta = \theta_i & \forall i \in [1, \dots, N] \\ 0 & \text{for } \theta = \theta_{j \neq i} & \forall i, j \in [1, \dots, N] \\ 1 - \frac{(\theta - \theta_i)}{(\theta_{i+1} - \theta_i)} & \text{for } \theta_i \leq \theta \leq \theta_{i+1} & \forall i \in [1, \dots, N] \\ 1 + \frac{(\theta - \theta_i)}{(\theta_{i-1} - \theta_i)} & \text{for } \theta_{i-1} \leq \theta \leq \theta_i & \forall i \in [1, \dots, N] \end{cases} \quad (3)$$

502 In general, it is advisable to instrument cross-sections forming equal angles between them so

503 that all the weight functions have the same periodicity in θ . Two sections are suggested as the

504 minimum number required for the procedure to work.

505 Analogously, with regard to the symmetrical part of the water content variation,

506 $w_k^s = w^s(x, s, z, t = t_k)$ is obtained as the weighted average of the values of water content,

507 $w_{i;k}^s = w^s(x, s = s_i, z, t = t_k)$, recorded in the N instrumented cross-sections at $t = t_k$:

508
$$w_k^s(x, s, z) = w^s(x, s, z, t = t_k) = \sum_{i=1}^N w_{i;k}^s(x, z) \cdot \beta_i(s) \quad (4)$$

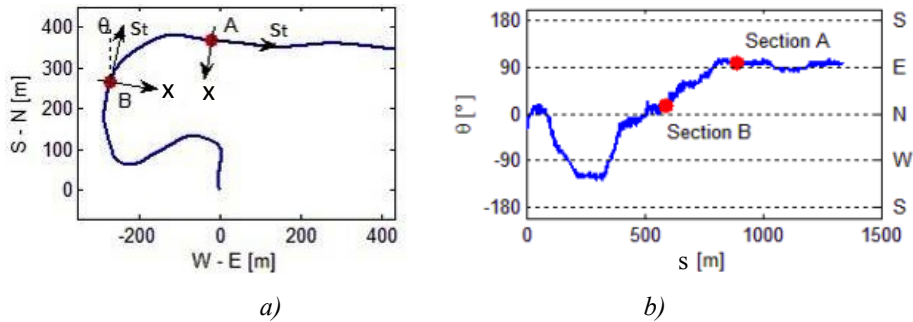
509 with $\beta_i(s)$ being weight functions that depend on s rather than θ . Considering again a linear

510 interpolation between the values of water content measured at the N instrumented sections as

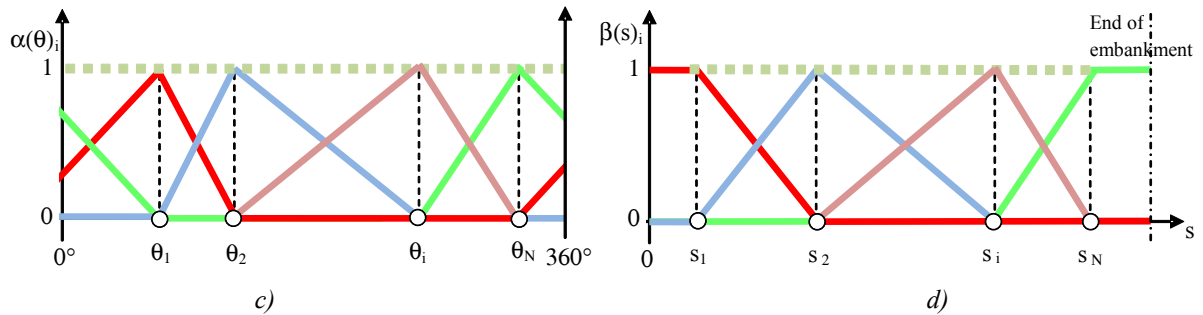
511 illustrated in Figure 12d, $\beta_i(s)$ are here defined as:

$$\beta_i(s) = \begin{cases} 1 & \text{for } s = s_i \quad \forall i \in [1, \dots, N] \\ 0 & \text{for } s = s_{j \neq i} \quad \forall i, j \in [1, \dots, N] \\ 1 - \frac{(s - s_i)}{(s_{i+1} - s_i)} & \text{for } s_i \leq s \leq s_{i+1} \quad \forall i \in [1, \dots, N] \\ 1 + \frac{(s - s_i)}{(s_{i-1} - s_i)} & \text{for } s_{i-1} \leq s \leq s_i \quad \forall i \in [1, \dots, N] \end{cases} \quad (5)$$

513 Unlike the case of the α_i functions, for $0 \leq s \leq s_1$, $\beta_1=1$ whilst for $s_N \leq s \leq L$, $\beta_N=1$ with L
514 being the total length of the embankment. This means that for $0 \leq s \leq s_1$,
515 $w^s(x, s, z, t = t_k) = w^s(x, s = s_1, z, t = t_k)$ whilst for $s_N \leq s \leq L$, $w^s(x, s, z, t = t_k) =$
516 $= w^s(x, s = s_N, z, t = t_k)$. This is because in the regions $0 \leq s \leq s_1$ and $s_N \leq s \leq L$, there is only
517 water content measurements are available only for 1 section so that no interpolation can be
518 carried out. Obviously in the choice of the location of the 1st and Nth cross-sections, care
519 should be taken to minimise the length of the longitudinal segments $s_1 - 0$ and $L - s_N$.



520
521



522
523

524 Figure 12. (a) plan view of the embankment layout; (b) orientation of the longitudinal axis of the embankment
525 with respect to the North; c) α weight functions against cross-section orientation; d) β weight functions against
526 longitudinal coordinate s .

527

528 The water content in any point of the embankment can now be obtained substituting Eqs.
 529 (3) and (5) into Eq. (1):

$$530 \quad w_k(x, s, z) = w(x, s, z, t = t_k) = \sum_{i=1}^N w_{i,k}^a(x, z) \cdot \alpha_i(\theta) + \sum_{i=1}^N w_{i,k}^s(x, z) \cdot \beta_i(s) \quad (6)$$

531 In our case $N=2$, so that $w_k(x, s, z)$ is calculated as:

$$532 \quad w_k(x, s, z) = w(x, s, z, t = t_k) = w^a(x, s = s_1, z, t = t_k) \cdot \alpha_1(\theta) + w^a(x, s = s_2, z, t = t_k) \cdot \alpha_2(\theta) +$$

$$533 \quad w^s(x, s = s_1, z, t = t_k) \cdot \beta_1(s) + w^s(x, s = s_2, z, t = t_k) \cdot \beta_2(s) \quad (7)$$

534 with 1 and 2 indicating sections A and B respectively. Note that Eq. (7) provides an analytical
 535 expression for the water content in any point of the embankment at the discrete time points t_k .
 536 So, provided that sufficiently small space intervals between instrumented cross-sections are
 537 employed and sufficiently small time intervals are used, the water content in the embankment
 538 could, in principle, be monitored as accurately as desired. So, one may be tempted to
 539 conclude that the use of the geotechnical suite alone is good enough for the health monitoring
 540 of the embankment. However, maintenance costs of the geotechnical suite over the typical
 541 lifespan of flood defence earth embankments (at least 50 years but more often 100-200 years)
 542 are higher than the costs for a monitoring programme based on geophysical measurements
 543 which only entail non-invasive periodic walk-over surveys. More importantly, only two
 544 sections have been used here. With regards to this point, in the authors' opinion, the proposed
 545 geotechnical suite may be employed as the only monitoring method, but in order to obtain
 546 accurate results, many more sections in the embankment should be monitored. If only a few
 547 sections are employed to keep the monitoring costs within affordable limits, geophysical
 548 probes are necessary to integrate the discrete geotechnical data with spatially continuous
 549 measurements acquired along the entire embankment. Such a procedure is detailed below.

550

551 **7.2 Integration of the geophysical data with the geotechnical suite**

552 Herein the variable σ will be employed to represent the ground electrical conductivity which
 553 is a function of both space and time, hence $\sigma = \sigma(x, s, z, t)$. However, electromagnetic
 554 probes provide a measure of σ which is averaged over a prismatic volume of ground where
 555 the induced electrical field is non-zero. Considering a generic cross-section of the
 556 embankment, we define:

$$557 \quad \bar{\sigma}(s, t) = \frac{\int_{A_{CMD}} w(x, s, z, t) dx dz}{A_{CMD}} \quad (8)$$

558 with $A_{CMD} = b \cdot d$, b being the distance between the two ends of the electromagnetic probe
 559 (hence corresponding to the width of the portion of the embankment cross-section where the
 560 induced electrical field is non-zero) and d the so-called effective depth, *i.e.* the depth of the
 561 induced electromagnetic field. Note that A_{CMD} is independent of the cross-section considered,
 562 *i.e.* its size does not vary with s , but depends on the type of electromagnetic probe employed
 563 (for this reason we called it A_{CMD}). The effective depth is a function of the type of ground and
 564 of the vertical distance from the portable device to ground level. d is an unknown that we
 565 determined by trial and error selecting the value which provides the best correlation between
 566 electrical conductivity and water content as illustrated later on (see Figure 14).

567 In Figure 13a, the measurements taken by the CMD-2 device at six time points along
 568 the entire embankment, $\bar{\sigma}_k(s) = \bar{\sigma}(s, t = t_k)$, are shown. It emerges that the shape of the
 569 curves is approximately the same for all the times considered. Now let us introduce the
 570 spatial average of $\bar{\sigma}(s, t)$ over the entire embankment length as:

$$571 \quad \bar{\bar{\sigma}}(t) = \frac{\int_{s=0}^{s=L} \bar{\sigma}(s, t) ds}{L} \quad (9)$$

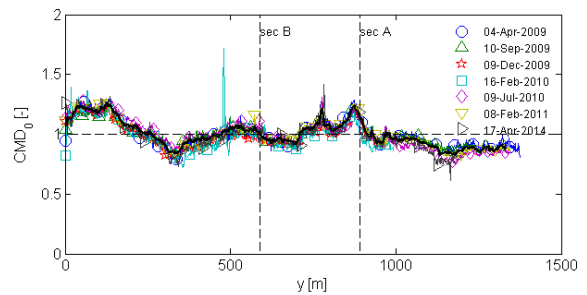
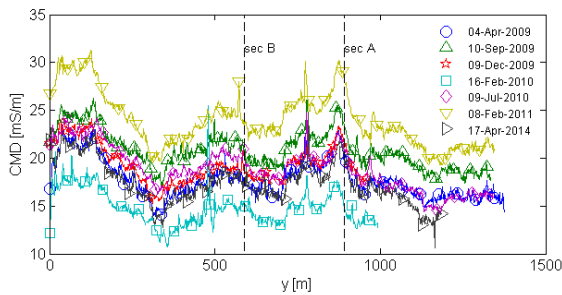
572 with the second above score bar denoting the spatial average over the longitudinal coordinate
 573 s . Then, we can introduce the normalised cross-sectional average electrical conductivity as:

$$574 \quad \bar{\sigma}_0(s, t) = \frac{\bar{\sigma}(s, t)}{\bar{\bar{\sigma}}(t)} \quad (10)$$

575 The normalised measurements taken at times t_k , *i.e.* $\bar{\sigma}_{0_k} = \bar{\sigma}_0(s, t = t_k)$, are plotted in Figure
 576 13b. From the figure, it emerges that the curves coincide almost perfectly. This leads to
 577 consider the average of $\bar{\sigma}_{0_k} = \bar{\sigma}_0(s, t = t_k)$ over time:

$$578 \quad \underline{\bar{\sigma}}_0(s) = \underset{k}{\text{average}} \bar{\sigma}_{0_k}(s, t = t_k) = \underset{k}{\text{average}} \left(\frac{\bar{\sigma}(s, t = t_k)}{\bar{\bar{\sigma}}(t = t_k)} \right) \quad (11)$$

579 as the representative curve of the conductivity of the embankment. Note that herein the
 580 underscore bar denotes time average. The measurements were taken by an operator walking
 581 above the centre of the embankment horizontal upper surface. Therefore, they cannot detect
 582 any conductivity variation due to different cross-section orientations, *i.e.* they are
 583 independent of the angle θ . The time-independent function $\underline{\bar{\sigma}}_0(s)$ can be thought of as a
 584 unique identifier of the embankment expressing the variation of conductivity along the s
 585 coordinate due to the variation of geometrical, hydraulic and lithological properties of cross-
 586 sections and to the effects of exposure to weather conditions independent of cross-section
 587 orientation, *i.e.* cross-sectionally symmetric. On the other hand, the function $\bar{\bar{\sigma}}(t)$ reflects the
 588 temporal effect of climatic variations (e.g. rainfall, wind, temperature variations, etc.) and
 589 aging on the ground conductivity.



590

591

a)

b)

592 *Figure 13. (a) electrical conductivity measurements along the embankments at seven different times; (b)*
 593 *normalised values of conductivity measurements.*

594

595 Now, we can split the ground conductivity function, $\bar{\sigma}(s,t)$, into the product of the
 596 time independent dimensionless function $\bar{\sigma}_0(s)$ with the space independent dimensional
 597 function $\bar{\bar{\sigma}}(t)$:

$$598 \quad \bar{\sigma}(s,t) = \bar{\sigma}_0(s) \cdot \bar{\bar{\sigma}}(t) \quad (12).$$

599 In the following it will be shown that this split is a necessary step to find a correlation
 600 between water content and electrical conductivity. First, let us define the average water
 601 content in the portion of the embankment cross-sections where the electromagnetic field is
 602 non-zero, *i.e.* A_{CMD} :

$$603 \quad \bar{w}(s,t) = \frac{\int_{A_{CMD}} w(x,s,z,t) dx dz}{A_{CMD}} \quad (13)$$

604 Analogously to $\bar{\sigma}(s,t)$, we can split $\bar{w}(s,t)$ into two functions: a time independent
 605 dimensionless function, $\bar{w}_0(s)$, which accounts for the effect of cross-section orientation and
 606 position on the ground water content and the space independent dimensional function, $\bar{\bar{w}}(t)$,
 607 which accounts for the effect of climatic variations and aging on the ground water content:

$$608 \quad \bar{w}(s,t) = \bar{w}_0(s) \cdot \bar{\bar{w}}(t) \quad (14).$$

609 $\bar{\bar{w}}(t)$ represents the spatial average of the water content on the cross-sectional area A_{CMD} and
 610 along the longitudinal coordinate s :

$$611 \quad \bar{\bar{w}}(t) = \frac{\int_0^L \frac{\int_{A_{CMD}} \left[\sum_{i=1}^N w^a(x,s=s_i,z,t) \cdot \alpha_i(\theta) + \sum_{i=1}^N w^s(x,s=s_i,z,t) \cdot \beta_i(s) \right] dx dz}{A_{CMD}} ds}{L} \quad (15)$$

612 To look for a correlation between the measured electrical conductivity and water content,
613 we shall consider the time dependent functions $\bar{w}(t)$ and $\bar{\sigma}(t)$. Before doing so, we need to
614 account for the strong dependency exhibited by the ground electrical conductivity on
615 temperature (Keller and Frischknecht, 1966). Recently Hayley et al., (2007) investigated this
616 dependency for a range of temperatures corresponding to our case (temperature varying
617 between 0 and 25 Celsius) on a glacial till finding a linear dependency of the type:

$$618 \quad \sigma = \sigma_{25} [C(T - 25) + 1] \quad (16)$$

619 with σ being the electrical conductivity measured at the temperature T and the constant
620 $C=0.02$. To account for the effect of temperature on the measured electrical conductivity, we
621 expressed all the measured values relative to the same reference temperature before
622 correlating them to the water content. As shown in (Hayley et al., 2007), manipulating Eq.
623 (16), the following expression for the calculation of σ relative to the chosen reference
624 temperature is obtained:

$$625 \quad \sigma_{ref} = \sigma \frac{1 + C(T_{ref} - 25)}{1 + C(T - 25)} \quad (17)$$

626 with σ_{ref} being the value of electrical conductivity relative to the reference temperature T_{ref} .
627 Here, we chose $T_{ref}=15$ Celsius to minimise the amount of temperature compensation.
628 Employing Eq. (17), we calculated σ_{ref} from the in-situ values of σ and T .

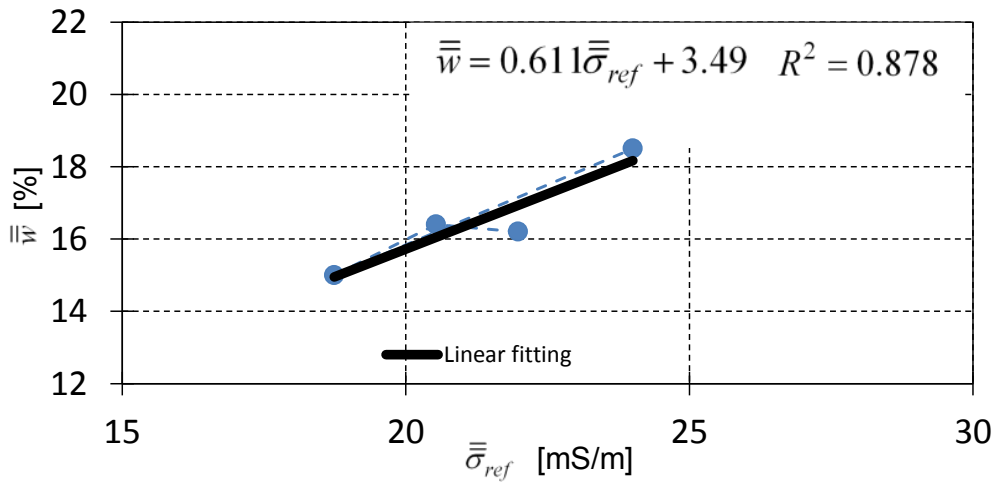
629 In Figure 14, the water content measured at the time points t_k , $\bar{w}(t = t_k)$ is plotted against
630 the electrical conductivity measured at the same time points, $\bar{\sigma}_{ref}(t = t_k)$. It emerges that the
631 relationship between $\bar{w}(t)$ and $\bar{\sigma}_{ref}(t)$ is well captured by a linear function so that:

$$632 \quad \bar{w}(t) = m\bar{\sigma}_{ref}(t) + q \quad (18)$$

633 with m and q determined by best fit (see Figure 14). Substituting Eq. (17) into Eq. (18), it
 634 becomes:

$$635 \quad \bar{w}(t) = m \bar{\sigma}(t) \frac{1 + C(T_{ref} - 25)}{1 + C(T - 25)} + q \quad (19).$$

636 Eq. (19) links the in-situ measured water content to the in-situ measured electrical
 637 conductivity.



638
 639 *Figure 14. Correlation obtained over the monitored 2 year time period between $\bar{\sigma}_{ref}$, electrical conductivity at*
 640 *the chosen reference temperature ($T_{ref}=15^{\circ}C$), and \bar{w} calculated for an effective depth of $d=0.2m$.*
 641

642 In order to work out the water content in any point of the embankment, $w(x,s,z,t)$, the
 643 space independent dimensional function $\bar{w}(t)$, must be multiplied by a normalised time
 644 independent function, $\underline{w}_0(x,s,z)$, so that:

$$645 \quad w(x,s,z,t) = \underline{w}_0(x,s,z) \cdot \bar{w}(t) \quad (20).$$

646 Following the approach adopted in par. 7.1, $w_0(x,s,z)$ is split into the summation of two
 647 parts, an anti-symmetrical and a symmetrical one:

$$648 \quad \underline{w}_0(x,s,z) = \underline{w}_0^a(x,s,z) + \underline{w}_0^s(x,s,z) \quad (21)$$

649 As in par. 7.1, we assume $\underline{w}_0^a(x, s, z)$ to be the time average of the linear combination of the
 650 functions expressing the normalised water content measured at times t_k at the N instrumented
 651 cross-sections, $w_{0_{i;k}}^a(x, z)$:

$$652 \quad \underline{w}_0^a(x, s, z) = \underset{k}{\text{average}} \left[\sum_{i=1}^N w_{0_{i;k}}^a(x, z) \cdot \alpha_i(\theta) \right] \quad (22)$$

653 According to standard normalisation procedures, $w_{0_{i;k}}^a(x, z)$ and $w_{0_{i;k}}^s(x, z)$ are defined as:

$$654 \quad w_{0_{i;k}}^a(x, z) = w_0^a(x, s = s_i, z, t = t_k) = \frac{w^a(x, s = s_i, z, t = t_k)}{\int_{A_i} w^a(x, s = s_i, z, t = t_k) dx dz}$$

$$655 \quad w_{0_{i;k}}^s(x, z) = w_0^s(x, s = s_i, z, t = t_k) = \frac{w^s(x, s = s_i, z, t = t_k)}{\int_{A_i} w^s(x, s = s_i, z, t = t_k) dx dz} \quad (23)$$

656 with A_i being the area of the i^{th} cross section.

657 For the symmetrical function $\underline{w}_0^s(x, s, z)$, we assume the following expression:

$$658 \quad \underline{w}_0^s(x, s, z) = \bar{w}^s(s, t) \cdot \bar{\sigma}_0(s) = \underset{k}{\text{average}} \left[\sum_{i=1}^N w_{0_{i;k}}^s(x, z) \cdot \beta_i(s) \right] \bar{\sigma}_0(s) \quad (24).$$

659 The dimensionless function $\bar{\sigma}_0(s)$ accounts for the spatial variation of water content along
 660 the longitudinal direction of the embankment detected by the geophysical probe during walk-
 661 over surveys. Eq. (24) constitutes an important improvement in comparison with Eq. (4) since
 662 the time average of the linear combination of the water content values measured at the N

663 instrumented cross sections, $\underset{k}{\text{average}} \left[\sum_{i=1}^N w_{0_{i;k}}^s(x, z) \cdot \beta_i(s) \right]$, is adjusted by multiplication with

664 $\bar{\sigma}_0(s)$ to account for the spatial variation of conductivity detected by the geophysical survey

665 along the longitudinal direction. The advantage of employing geophysics is now apparent

666 since it provides measurements which are continuous along the spatial coordinate s . This

667 allows improving the quality of the estimated water content especially in the zones of the
 668 embankment farthest away from the geotechnically instrumented cross-sections.

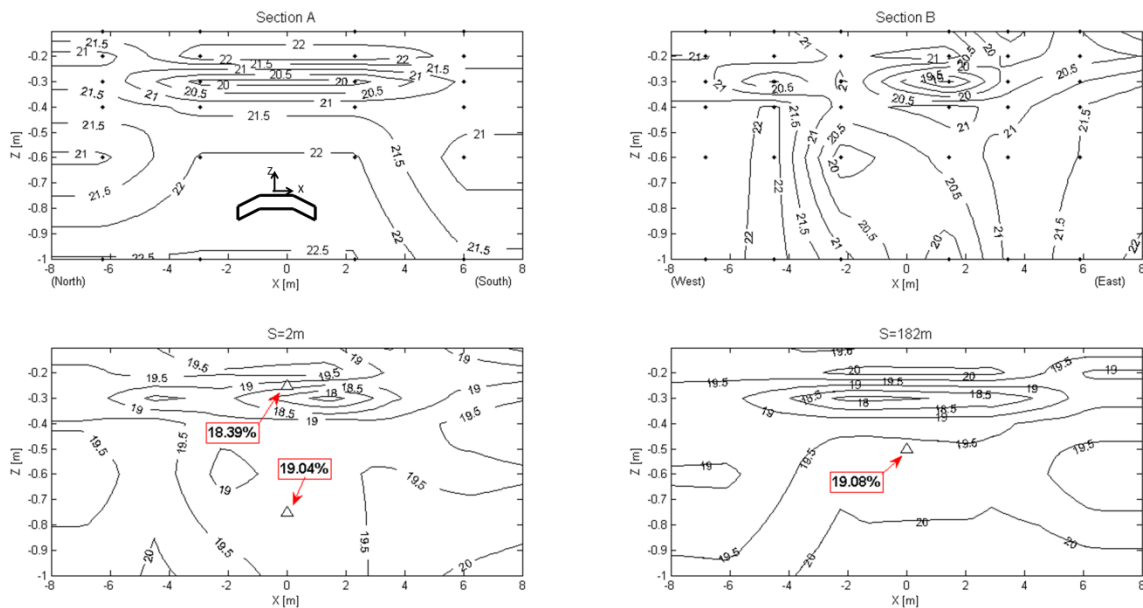
669 So far the symmetrical component of the water content, $w_0^s(x,s,z)$ has been related to
 670 the geophysical measurements of the variation of ground electrical conductivity along the s
 671 coordinate, *i.e.* dependent on cross-section position. In principle it should also be possible to
 672 relate the anti-symmetrical component of the water content $w_0^a(x,s,z)$ to geophysical
 673 measurements of the variation of ground electrical conductivity due to cross-section
 674 orientation, *i.e.* dependent on the angle θ . Let us recall that the geophysical measurements
 675 were taken by an operator walking above the centre of the embankment horizontal upper
 676 surface where the effect of cross-section orientation is negligible so that the measurements
 677 are a function of cross-section position only (hence of the s coordinate only). To correlate
 678 electrical conductivity to the anti-symmetrical part of the water content, measurements of
 679 electrical conductivity along more than one path would be needed with some of them being
 680 along the embankment flanks. However, these measurements would be likely affected by a
 681 large error since it is very difficult to walk for long distances on the embankment flanks
 682 (which are variously inclined), keeping a constant geometrical height (z coordinate).

683 Now, substituting Eq. (19), (22) and (24) into Eq. (20), the water content at the time t_l of
 684 the geophysical measurement $w(x,s,z,t=t_l)$, can be derived as a function of the average
 685 cross-sectional ground conductivity, $\bar{\sigma}(s,t=t_l)$:

$$\begin{aligned}
 & 686 \quad w(x,s,z,t=t_l) = \left\{ \text{average} \left[\sum_{i=1}^N w_0^a(x,s=s_i,z,t=t_k) \cdot \alpha_i(\theta) \right] + \text{average}_k \left[\sum_{i=1}^N w_0^s(x,s=s_i,z,t=t_k) \cdot \beta_i(s) \right] \cdot \bar{\sigma}_0(s) \right\} \cdot \\
 & 687 \quad \left(m \frac{\bar{\sigma}(s,t=t_l)}{\bar{\sigma}_0(s)} \frac{1 + C(T_{ref} - 25)}{1 + C(T - 25)} + q \right) \quad (0).
 \end{aligned}$$

688 Eq. (25) provides the analytical expression to be employed to monitor the water content in the
 689 embankment carrying out periodic walk-over surveys over a time period which can be much
 690 longer than the time of activity of the geotechnical suite (*i.e.* $t_l > t_k$).

691 The spatial distributions of the water content calculated using Eq. (25) in four cross-
 692 sections ($s = 2, 182, 672$ and 972m) from the electrical conductivity profile of the
 693 embankment, measured during a walk-over survey carried out on 17th April 2014 (so for
 694 $t_l > t_k$), are plotted in Figure 15. In order to provide a validation of the proposed method, a
 695 few soil samples were retrieved from the embankment and brought to the laboratory for
 696 accurate measurement. In the plots of Figure 15c and d, the experimental values of water
 697 content are reported as triangles. Comparing the predictions of the method with the
 698 experimental measurements of water content, the predictions show to be in very good
 699 agreement with the experimentally measured values. This is quite remarkable especially in
 700 light of the fact that the measurements were taken at a time (17th April 2014) well beyond the
 701 2 year period within which the geotechnical and geophysical measurements had been
 702 performed to calibrate the model.



703

704 *Figure 15. values of the water content estimated from the electrical conductivity measured by the CMD-2 during*
705 *a walk over survey carried out on 17th April 2014 employing the proposed methodology . a) water content in*
706 *section A; b) water content in section B; c) water content at s=2m; d) water content at s=182.The triangles in*
707 *figures c) and d) indicate the value of water content measured in the laboratory from the retrieved in-situ*
708 *samples.*

709

710 **7.3 Options for long term monitoring**

711 In light of our results, three options of increasing accuracy but also requiring increasing costs
712 emerge for the monitoring of the embankment water content over time. The first and cheapest
713 option consists of using meteorological data only; the second more expensive option relies on
714 periodic walk-over surveys to retrieve geophysical data employing electromagnetic probes;
715 the third most expensive option requires both periodic walk-over surveys to retrieve
716 geophysical data and measurements in a number of cross-sections from a permanent
717 geotechnical suite. The first option requires the use of the geotechnical suite for an initial
718 limited period of time without any periodic (geotechnical or geophysical) measurement at
719 subsequent times. In the second option, the integration of geotechnical data with geophysical
720 ones (section 7.2) is carried out in a first limited initial period only whereas in the third option
721 it is carried out repeatedly during the whole lifetime of the structure. The second option
722 provides predictions more robust than the first one since the first option relies on a
723 relationship between meteorological data and variation of the water content established over
724 the initial time of monitoring which is expected to change over time with the ageing of the
725 structure. Depending on the importance of the structure and the available financial resources,
726 the authorities in charge of the maintenance of the embankments can select the most suitable
727 option.

728

729 **8. A proposal for a susceptibility index to desiccation fissuring**

730 Here, a proposal for a susceptibility index for a failure mechanism that can be directly related
731 to the presence of desiccation cracks is put forward. Cooling and Marsland, (1953), Marsland
732 and Cooling, (1958) and more recently Morris et al., (2007) and Dyer et al., (2009) have
733 described failure mechanisms which take place when water overflows the embankment crest
734 in the presence of an interconnected pattern of vertical and horizontal cracks underneath the
735 horizontal upper surface and the landward flank of the embankment. Overtopping water
736 seeping downwards into the open cracks leads to the progressive uplift and removal of intact
737 blocks of ground, first from the landward flank and subsequently from the horizontal upper
738 surface. This failure mechanism is particularly dangerous since it leads to the development of
739 a fast breach which can lead to quick flooding. The formation of extensive cracks is also
740 detrimental for the structure since it favours internal piping.

741 Tests run by Tang et al., (2012) on clay samples of various shape show that after 4
742 wetting-drying cycles, the onset of cracks can be uniquely related to the value of the soil
743 water content, *i.e.* it becomes independent of the wetting-drying history. In Costa et al.
744 (2013), it is shown that once the water content in clayey soils lowers below a threshold value
745 near the plastic limit, $w_{plastic}$, no additional cracks are formed. The determination of a
746 threshold value of water content at which an interconnected network of cracks is formed and
747 equally the determination of a critical threshold value for piping failure are challenging issues
748 outside of the scope of this paper. Unsaturated soil mechanics and the formation of
749 desiccation fissures in cohesive soils are topics of intense current research. Therefore, it is
750 plausible to expect that in the future, with further results becoming available, it will be
751 possible to establish a better susceptibility index based on less crude assumptions. The index
752 here proposed has been conceived to provide a purely qualitative indication about which
753 zones of the embankment are liable to fissuring; so it has not to be relied upon for

754 quantitative predictions on the level of hazard, or on the likelihood of failure in these zones.
755 Here, for sake of simplicity, we assumed this threshold to coincide with the plastic limit
756 ($w_{plastic}$) of the till. As a first approximation, we also assumed that the ground zones where the
757 water content is below the plastic limit are fissured so that the portion of cross section where
758 $w < w_{plastic}$ is considered fully fissured; whereas the portion where $w > w_{plastic}$ is considered
759 intact. The sought susceptibility index has to reflect how far a cross-section is from the
760 critical condition leading to failure. Hence, the index here proposed is defined as the ratio of
761 the sectional area where cracks have formed, A_{fis} , over the sectional area required for the
762 development of the considered failure mechanism, A_{Ω} :

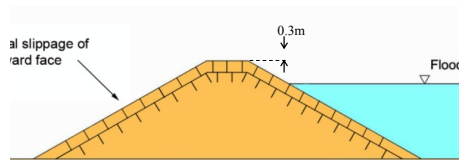
$$763 \quad I = \frac{A_{fis}}{A_{\Omega}} \quad \text{with } 0 < I < 1 \quad (26)$$

764 The size of A_{Ω} is a property of the ground. In Dyer et al. (2009), a maximum characteristic
765 depth for the formation of an interconnected network of cracks 0.6 m deep was observed in
766 trial pits excavated in embankments made of glacial tills similar to the embankment
767 investigated in our paper. Therefore, a depth of 0.6 m was used to determine the sectional
768 domain employed for the calculation of A_{Ω} (see Figure 16a).

769 In Figure 16b, the function $I(s)$ representing the value of the index along the
770 embankment, has been plotted for two different time points. It can be observed that in winter
771 the susceptibility index is nil (*i.e.* no fissuring is expected) in most of the embankment, apart
772 from two rather small zones where the index spikes up to 1. Conversely in summer, the index
773 assumes values larger than 0 in the whole embankment. Figure 16b is sufficient to identify
774 the zones of the embankment which are most in need of remedial measures. However, it may
775 be useful to define categories of risk for intervention protocols whereby the type of
776 intervention and its urgency are related to the established categories. Here, as an example,
777 three categories were established: no risk (green color) associated to $0 < I < 0.5$, moderate risk

778 (yellow color) associated to $0.5 < I < 0.90$, and high risk (red color) associated to $0.90 < I < 1$. In
 779 the zones classed as high risk ($I > 0.9$), cracks were observed during both the winter and the
 780 summer period (see Figure 16e). Also, the plots in Figure 16c and d provide a user-friendly
 781 visualisation of the location of the most critical zones in the embankment.

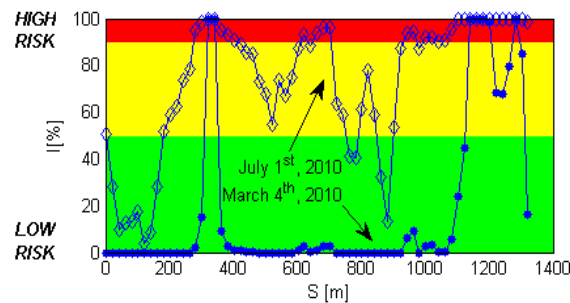
782



783

784

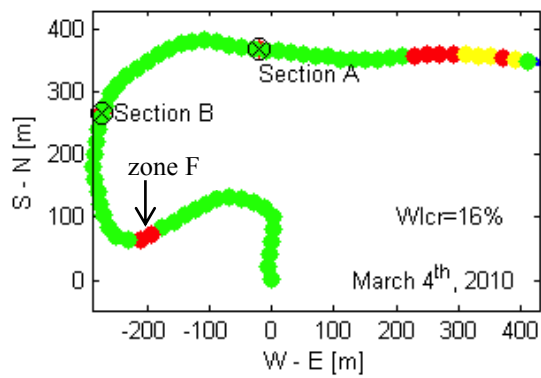
a)



785

786

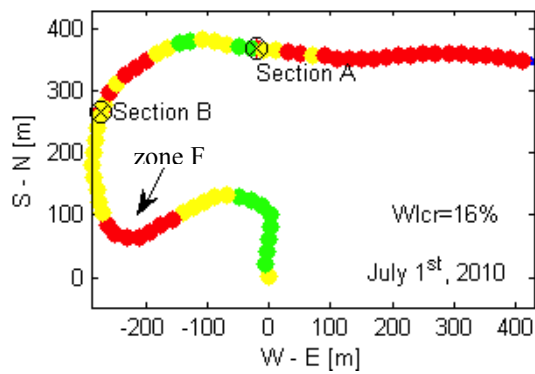
b)



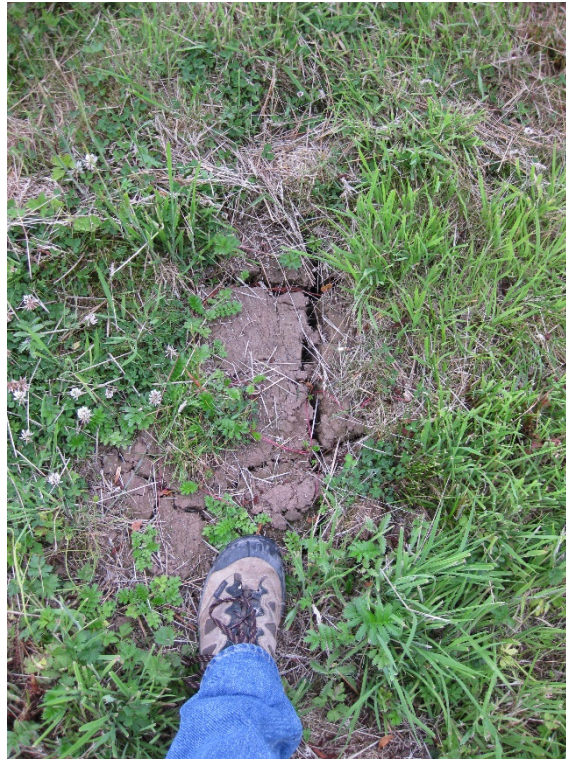
787

788

c)



d)



e)

789

790

791 *Figure 16. (a) representation of the total area A_{Ω} considered in the calculation of the susceptibility index (figure*
792 *modified from Dyer et al., 2009); (b) comparison between the calculated susceptibility index along the*
793 *embankment on March 4th and July 1st, 2010; (c) and (d) risk map of the embankment drawn on March 4th and*
794 *on July 1st, 2010; (e) picture of a surficial crack system taken in zone F of Figures c and d.*

795

796 **9. Conclusions**

797 In this paper, a cost effective methodology for the quantitative assessment of the potential for
798 desiccation fissuring for earthen embankments and tailing dams was established. Currently,
799 monitoring and condition assessment of embankments is performed by visual inspections at
800 set intervals. The proposed methodology is simple and suitable to be employed over the
801 entire lifetime of the structures by the authorities in charge of their maintenance. This
802 methodology paves the way for a radical improvement from the methods currently employed
803 moving to a quantitative assessment of the liability of long embankments (levees) to
804 desiccation fissuring.

805 The methodology is based on the use of a suite of standard geotechnical probes for the
806 measurement of the water content in a limited number of locations in the embankment
807 integrated with periodic non-invasive geophysical measurements from walkover surveys
808 employing portable electromagnetic probes. Most of the data from the geotechnical suite
809 were acquired by automatic reading systems involving minimal manpower. An innovative
810 calibration procedure was employed to calibrate the geotechnical probes (theta probe, profile
811 probe, diviner, etc.) in-situ by cross-comparison.

812 An index of susceptibility to desiccation induced deterioration was defined. Contour plots
813 of the calculated index provide an easy-to-be-used visual tool to monitor the health state of
814 the structure and identify the most critical zones to prioritise remedial interventions. Also a
815 protocol to monitor the susceptibility of earthen embankments to desiccation induced
816 deterioration over their lifespan is proposed based on three hierarchical levels of increasing
817 cost but also of increasing accuracy. The first and cheapest option consists of using
818 meteorological data only; the second more expensive option relies on periodic walk-over
819 surveys to retrieve geophysical data from the site; whereas the third most expensive option
820 requires both measurements in a number of cross-sections from a permanent geotechnical
821 suite and periodic walk-over surveys to retrieve geophysical data.

822

823 **Acknowledgements**

824 This research was carried out within the project “Long term deterioration of flood
825 embankments” funded by the Scottish Executive and by grant 0708 from the ICE Research
826 and Development Enabling Fund. Mr Marco Secondi is thanked for his help in setting out the
827 instrumentation and acquiring and managing the database from the field. Ms Chiara Grisanti
828 is thanked for contributing to obtain figures 9, 10 and 15 from her Bachelor thesis.

829

830 **Notation**

831	i	integer indicating the number of the embankment cross section considered
832	k	integer indicating the chronological sequence of the measurement performed
833	m	slope coefficient for linear interpolation in Figure 14
834	q	intercept coefficient for linear interpolation in Figure 14
835	x	local Cartesian horizontal coordinate in the embankment cross-section
836	s	global curvilinear coordinate along the longitudinal axis of the embankment
837	s_t	local Cartesian coordinate orthogonal to x and z
838	z	local vertical downward Cartesian coordinate
839	P	vertical line (point on the embankment surface) in the cross section B of the embankment
840	X	global Cartesian coordinate
841	Y	global Cartesian coordinate
842	Z	global Cartesian coordinate
843	$w(x, s, z, t)$	water content
844	$w_{plastic}$	water content at the plastic limit
845	$w^s(x, s, z, t)$	symmetrical part of the cross-sectional water content
846	$w^a(x, s, z, t)$	anti-symmetrical part of the cross-sectional water content
847	$w_k = w(x, s, z, t = t_k)$	water content measured at the time t_k
848	$w_{i,k} = w(x, s = s_i, z, t = t_k)$	water content measured in cross-section i at time t_k
849	$w_p = w(x = x_p, s = s_p, z, t)$	water content measured along the vertical line P
850	$\bar{w}(s, t)$	cross-sectional water content average. The water content is averaged over the portion of embankment
851		cross-section where the induced electric field is non zero (A_{CMD})

- 852 $\bar{w}(t)$ space average of the water content (average over the entire embankment). The water content is
853 averaged over the portion of embankment cross-section where the induced electric field is non zero (A_{CMD})
- 854 $\bar{w}_0(s,t)$ normalised cross-sectional average water content
- 855 $\bar{w}_0(s)$ time average of the normalised cross-sectional average water content
- 856 α weight function
- 857 β weight function
- 858 θ angle of s_t with the X axis. It indicates the orientation of a cross-section with regard to the global
859 Cartesian coordinate system
- 860 σ electrical conductivity
- 861 $\bar{\sigma}(s,t)$ cross-sectional average electrical conductivity. The electrical conductivity is averaged over the portion
862 of embankment cross-section where the induced electric field is non zero (A_{CMD})
- 863 $\bar{\sigma}_k(s) = \bar{\sigma}(s,t = t_k)$ cross-sectional electrical conductivity average measured at the time t_k
- 864 $\bar{\bar{\sigma}}(t)$ space average of the electrical conductivity (average over the entire embankment). The electrical
865 conductivity is averaged over the portion of embankment cross-section where the induced electric field is non
866 zero (A_{CMD})
- 867 $\bar{\sigma}_0(s,t)$ normalised cross-sectional average electrical conductivity.
- 868 $\bar{\sigma}_0(s)$ time average of the normalised cross-sectional average electrical conductivity
- 869 A_{CMD} portion of cross-sectional area where the induced electric field is non-zero.
- 870 A_{Ω} portion of cross-sectional area with interconnected cracks causing a decrease of bearing capacity
- 871 A_{fis} portion of the cross-sectional area where $w < w_{plastic}$
- 872 A_i area of cross-section i
- 873 C constant
- 874 I susceptibility index

876 **References**

- 877 1. Allsop W., Kortenhaus A., Morris M., Buijs F., Hassan R., Young M., Doorn N., der Meer
878 J., Van Gelder P., Dyer M., Redaelli M., Utili S., Visser P., Bettess R., Lesniewska D.,
879 Horst W. (2007). Failure mechanisms for flood defence structures. EU FP7 FLOODSite
880 task 4, Research Report: T04-06-01.
- 881 2. Andersen G.R., Chouinard L.E., Bouvier C., Back W.E. (1999). Ranking procedure on
882 maintenance tasks for monitoring of embankment dams. *Journal of Geotechnical and*
883 *Geoenvironmental Engineering*, **125**, 247-259.
- 884 3. Aubeny C.P., Lytton R.L. (2004). Shallow slides in compacted high plasticity clay slopes.
885 *J Geotech & Geoenv Engrg ASCE*, **130**, 717-727.
- 886 4. Charles J.A. (2008). The engineering behaviour of fill materials: the use, misuse and
887 disuse of case histories. *Geotechnique*, **58**, 541-570.
- 888 5. Cooling L.F., Marsland A. (1953). Soil mechanics studies of failures in the sea defence
889 banks of Essex and Kent. *Proceedings of the ICE Conference on the North Sea Floods of*
890 *31 January/1 February 1953*, ICE, London, 58–73.
- 891 6. Costa S., Kodikara J., Shannon B. (2013). Salient factors controlling desiccation cracking
892 of clay in laboratory experiments. *Geotechnique*, **63**: 18-29.
- 893 7. D’Elisio C. (2007). Breaching of sea dikes initiated by wave overtopping: A tiered and
894 modular modeling approach. Ph.D. thesis, Univ. of Braunschweig, Germany, and Univ. of
895 Florence, Italy.
- 896 8. De Vita P., Di Maio R., Piegari E. (2012). A study of the correlation between electrical
897 resistivity and matric suction for unsaturated ash-fall pyroclastic soils in the Campania
898 region (southern Italy). *Environmental Earth Science*, DOI 10.1007/s12665-012-1531-4.

- 899 9. Di Maio R., Piegari E. (2011). Water storage mapping of pyroclastic covers through
900 electrical resistivity measurements. *Journal of Applied Geophysics* **75**, 196-202.
- 901 10. Dyer M., Utili S., Zielinski M. (2009). Field survey of desiccation fissuring of flood
902 embankments. *Proc. ICE Water Management* **162**, 221-232.
- 903 11. Environment Agency (2006). Condition assessment manual. Report DR 166_03_SD01
- 904 12. Gf Instruments (2011). Short guide for electromagnetic conductivity survey.
905 (www.gfinstruments.cz).
- 906 13. GID (2014). GID reference manual. Available at www.gidhome.com/support/manuals.
- 907 14. Hayley K., Bentley L.R., Gharibi M., Nightingale M. (2007). Low temperature
908 dependence of electrical resistivity: implications for near surface geophysical monitoring.
909 *Geophysical Research Letters*, **34**: L18402.
- 910 15. Keller G.V., Frischknecht F.C., (1966). *Electrical Methods in Geophysical Prospecting*.
911 Pergamon Press, Oxford, 517p.
- 912 16. Konrad JM., Ayad R. (1997). Desiccation of a sensitive clay: field observations. *Canadian*
913 *Geotechnical Journal*, **34**: 929–942.
- 914 17. Marsland A., Cooling L.F. (1958). Tests on Full Scale Clay Flood Bank to Study Seepage
915 and the Effects of Overtopping. Building Research Station, Watford, Internal report No.
916 C562.
- 917 18. Milly P., Wetherald R., Dunne K., Delworth T. (2002). Increasing risk of great floods in a
918 changing climate. *Nature*, **415**(6871), 514–517.
- 919 19. Morris M., Dyer M., Smith P., Falkingham J., Simms J. (2007). Management of Flood
920 Defences. Defra/EA, R&D report FD2411, London.

- 921 20. Munoz-Castelblanco J.A., Pereira J.M., Delage P., Cui Y.J. (2012a). The Influence of
922 Changes in Water Content on the Electrical Resistivity of a Natural Unsaturated Loess.
923 *Geotechnical Testing Journal*, **35**(1): 11-17.
- 924 21. Munoz-Castelblanco J.A., Pereira J.M., Delage P., Cui Y.J. (2012b). The water retention
925 properties of a natural unsaturated loess from northern France. *Geotechnique*, **62**, 95-106.
- 926 22. Perry J., Pedley M., Reid M. (2001). Infrastructure embankment: condition appraisal and
927 remedial treatment. CIRIA Report C550.
- 928 23. Rodriguez R., Sanchez M., Ledesma A., Lloret A. (2007) Experimental and numerical
929 analysis of desiccation of a mining waste. *Canadian Geotechnical Journal*, **44**(6): 644-
930 658.
- 931 24. Shin H., Santamarina JC. (2011). Desiccation cracks in saturated fine-grained soils:
932 particle level phenomena and effective stress analysis. *Geotechnique* **61**, 11, 961-972.
- 933 25. Smethurst J.A., Clarke D., Powrie W. (2012). Factors controlling the seasonal variation in
934 soil water content and pore water pressures within a lightly vegetated clay slope.
935 *Geotechnique*, **62**(5), 429-446.
- 936 26. Tang CS., Cui YJ., Shi B., Tang AM., Liu C. (2011). Desiccation and cracking behaviour
937 of clay layer from slurry state under wetting-drying cycles. *Geoderma*, **166**: 111-118.
- 938 27. Utili S. (2013). Investigation by limit analysis on the stability of slopes with cracks.
939 *Geotechnique*, **63**(2), 140-154.
- 940 28. Xu C.Y., Singh V.P. (2001). Evaluation and generalization of temperature-based methods
941 for calculating evaporation. *Hydrological Processes*, 15(2): 305-319.
- 942 29. Wan C.F., Fell R. (2004). Investigation of rate erosion of soils in embankment dams. *J. of*
943 *Geoenv. and Geotech. Engrg ASCE*, **130**, (4), 373-380.
- 944 30. Wu W. et al. (2011). Earthen embankment breaching. *Journal of Hydraulic Engineering*
945 *ASCE*, **137**, 1549-1564.

- 946 31. Zhang Z., Tao M., Morvant M. (2005). Cohesive slope surface failure and evaluation. *J*
947 *Geotech & Geoenv Engrg ASCE*, **131**, 898-906.
- 948 32. Zielinski M. (2009). Influence of desiccation fissuring on the stability of flood
949 embankments. PhD thesis, University of Strathclyde, Glasgow (UK).
- 950 33. Zielinski M., Sanchez M., Romero E., Sentenac P. (2011). Assessment of water retention
951 behaviour in compacted fills. *Proc. ICE Geotechnical Engineering*, **164**, 139-148.